JOURNAL OF GEOPHYSICAL RESEARCH, VOL. 108, NO. B7, 2354, doi:10.1029/2002JB002311, 2003

Magma supply dynamics at Westdahl volcano, Alaska, modeled from satellite radar interferometry

Zhong Lu,[1] Timothy Masterlark,[1] Daniel Dzurisin,[2] Russell Rykhus,[1] and Charles Wicks Jr.[3]

Received 15 November 2002; revised 19 March 2003; accepted 2 April 2003; published 31 July 2003.

[1] A group of satellite radar interferograms that span the time period from 1991 to 2000 shows that Westdahl volcano, Alaska, deflated during its 1991–1992 eruption and is reinflating at a rate that could produce another eruption within the next several years. The rates of inflation and deflation are approximated by exponential decay functions having time constants of about 6 years and a few days, respectively. This behavior is consistent with a deep, constant-pressure magma source connected to a shallow reservoir by a magma-filled conduit. An elastic deformation model indicates that the reservoir is located about 6 km below sea level and beneath Westdahl Peak. We propose that the magma flow rate through the conduit is governed by the pressure gradient between the deep source and the reservoir. The pressure gradient, and hence the flow rate, are greatest immediately after eruptions. Pressurization of the reservoir decreases both the pressure gradient and the flow rate, but eventually the reservoir ruptures and an eruption or intrusion ensues. The eruption rate is controlled partly by the pressure gradient between the reservoir and surface, and therefore it, too, decreases with time. When the supply of eruptible magma is exhausted, the eruption stops, the reservoir begins to repressurize at a high rate, and the cycle repeats. This model might also be appropriate for other frequently active volcanoes with stable magma sources and relatively simple magma storage systems. *INDEX TERMS:* 1299 Geodesy and Gravity: General or miscellaneous; 6924 Radio Science: Interferometry; 8414 Volcanology: Eruption mechanisms; 8419 Volcanology: Eruption monitoring (7280); 8494 Volcanology: Instruments and techniques; *KEYWORDS:* interferometric synthetic aperture radar, InSAR, Westdahl volcano, deformation dynamics, volcano monitoring

Citation: Lu, Z., T. Masterlark, D. Dzurisin, R. Rykhus, and C. Wicks Jr., Magma supply dynamics at Westdahl volcano, Alaska, modeled from satellite radar interferometry, *J. Geophys. Res.*, *108*(B7), 2354, doi:10.1029/2002JB002311, 2003.

1. Introduction

[2] Surface deformation patterns can provide important insights into the structure, plumbing, and state of restless volcanoes [e.g., *McNutt et al.*, 2000]. Most eruptions are preceded by measurable ground deformation caused by pressurization of a magma reservoir or by upward intrusion of magma. The sense of ground movement often reverses, typically from uplift to subsidence, as the reservoir pressure decreases during the eruption, then reverses again when the reservoir starts to repressurize [e.g., *Dvorak and Dzurisin*, 1997; *Dzurisin*, 2003]. Deformation patterns before, during, and after eruptions or intrusions, together with seismicity, gas emission, and other indicators, provide a basis for understanding how volcanoes behave and ultimately forecast their activity.

[3] By analogy with the earthquake cycle in seismology, we can conceptualize an ‘‘eruption cycle’’ from deep magma generation through surface eruption, including such stages as partial melting, initial ascent through the upper mantle and lower crust, crustal assimilation, magma mixing, degassing, shallow storage, and final ascent to the surface [*Dzurisin*, 2003]. Not all stages are represented in every event. For example, some eruptions apparently are fed from shallow magma bodies that might not be replenished before every eruption, and others produce primitive lavas that show no evidence of storage, assimilation, or mixing. Some intrusions crystallize before they reach the surface and therefore might not advance the cycle toward the next eruption. The timescale for magma generation, ascent, and storage is poorly constrained and is variable from one eruption to the next. In some cases, the early part of the cycle is relatively brief (e.g., rapid ascent of magma from a deep source directly to the surface) or the latter part is protracted (e.g., long periods of storage, assimilation, and crystallization between eruptions of large silicic caldera systems). As a result of such complexities, deformation patterns vary considerably both during the eruption cycle and from volcano to volcano [*Dvorak and Dzurisin*, 1997]. Recent advances in geodetic monitoring, including continuous Global Positioning System (GPS) recordings, borehole

---

[1] U.S. Geological Survey, EROS Data Center, SAIC, Sioux Falls, South Dakota, USA.

[2] U.S. Geological Survey, David A. Johnston Cascades Volcano Observatory, Vancouver, Washington, USA.

[3] U.S. Geological Survey, Menlo Park, California, USA.

Published in 2003 by the American Geophysical Union.

strainmeters and tiltmeters, and interferometric synthetic aperture radar (InSAR), make it possible to better characterize volcano deformation patterns both spatially and temporally [*Dzurisin*, 2003].

[4] In this paper, we document and model deformation patterns at Westdahl volcano, Alaska, using InSAR images acquired from 1991 to 2000, including time windows before, during, and after an eruption in 1991–1992. From the spatial pattern, we identify the location and capacity of a magma reservoir beneath the volcano, and from the temporal pattern, we infer the configuration of the plumbing system and dynamics of reservoir filling. A model based on those constraints accounts for Westdahl's recent behavior and might be applicable to other volcanoes as well.

1.1. InSAR Studies of Alaskan Volcanoes

[5] InSAR has become an important technique for studying volcanoes, because it can be used to map deformation with centimeter to subcentimeter precision at a spatial resolution of tens of meters and to produce digital elevation models (DEMs) with a vertical precision of several meters [*Massonnet and Feigl*, 1998; *Rosen et al.*, 2000; *Zebker et al.*, 2000]. Deformation has been observed with InSAR at many volcanoes worldwide [e.g., *Massonnet et al.*, 1995; *Lu et al.*, 1997, 1998, 2000a, 2000b, 2000c, 2002a, 2002b, 2002c; *Sigmundsson et al.*, 1997, 1999; *Thatcher and Massonnet*, 1997; *Fujiwara et al.*, 1998; *Lanari et al.*, 1998; *Wicks et al.*, 1998, 2002; *Jonsson et al.*, 1999; *Amelung et al.*, 2000; *Beauducel et al.*, 2000; *Zebker et al.*, 2000], and InSAR DEMs have been used to study the volumes and surface movements of young lava flows [*Stevens et al.*, 2001; *Hensley et al.*, 2001; *Lu et al.*, 2003a].

[6] Most InSAR studies of volcanoes have used C-band SAR images collected by the European Space Agency's ERS-1 and ERS-2 satellites (wavelength $\lambda = 5.7$ cm). Major factors that limit the usefulness of C-band InSAR data are atmospheric delay anomalies and loss of interferometric coherence. A common strategy to deal with atmospheric delay anomalies is to use multiple interferograms that span similar time intervals to qualitatively distinguish the anomalies from surface deformation. Atmospheric delay anomalies might be removed using the permanent scattering InSAR technique [*Ferretti et al.*, 2000]. Loss of interferometric coherence can be partly avoided by using longer-wavelength L-band radars ($\lambda \sim 24$ cm) such as those on the Japanese JERS-1 satellite [*Murakami et al.*, 1996] and the proposed Japanese ALOS satellite.

[7] InSAR has been used to study both eruptive and noneruptive activity at several volcanoes in the Aleutian volcanic arc (Figure 1a) [*Lu et al.*, 2003b]. Examples include preeruptive inflation, coeruptive deflation, and posteruptive inflation at Okmok volcano [*Lu et al.*, 2000a; *Mann et al.*, 2002]; magmatic intrusion and associated tectonic strain release at Akutan volcano [*Lu et al.*, 2000c]; magmatic intrusion at Mount Peulik volcano and its relation to an earthquake swarm 30 km away [*Lu et al.*, 2002a]; magmatic intrusion at Makushin volcano associated with a small eruption in 1995 [*Lu et al.*, 2002b]; surface subsidence caused by a decrease in pore fluid pressure in an active hydrothermal system beneath Kiska volcano [*Lu et al.*, 2002c]; compaction of young pyroclastic flow deposits at Augustine volcano [*Lu et al.*, 2002d; *Lu et al.*, 2003b]; complex patterns of transient deformation during and after the 1992–1993 eruption at Seguam volcano [*Lu et al.*, 2003b]; lack of expected deformation associated with recent eruptions at Shishaldin, Pavlof, Cleveland, and Korovin volcanoes [*Lu et al.*, 2003b]; and the volumes of young lava flows at Okmok volcano calculated by differencing precise DEMs [*Lu et al.*, 2003a].

1.2. InSAR Studies of Westdahl Volcano

[8] *Lu et al.* [2000b] produced six interferograms of Westdahl volcano that revealed surface uplift of as much as 17 cm from 1993 to 1998. The uplift rate was greater from 1993 to 1995 than from 1995 to 1998. Given the volume of inflation (0.05 km^3) and the timing and volume of recent eruptions, Lu et al. noted that another event could be expected within the next several years. Since the Alaska Volcano Observatory installed a local seismic network at Westdahl in 1998, the background level of seismicity has been low [*Jolly et al.*, 2001].

[9] For this study, we systematically produced interferograms from all suitable SAR images of Westdahl acquired by the ERS-1 and ERS-2 satellites from 1991 to 2000 and then modeled the observed deformation. In this paper, we (1) discuss our results for the location of a magma reservoir and its inflation rate as a function of time, (2) compare the volume of inflation since the 1991–1992 eruption to the lava volumes extruded during the 1964 and 1991–1992 eruptions, (3) propose a physically based model for the magma plumbing system, and (4) discuss implications for eruption prediction.

1.3. Westdahl Volcano and its Recent Eruptions

[10] Westdahl is a young glacier-capped shield volcano located on the west end of Unimak Island, in the central part of the Aleutian volcanic arc, and about 85 km southwest of the tip of the Alaska Peninsula (Figure 1a). The Westdahl edifice is composed of a thick sequence of preglacial basalt lava flows. The most active historical vent is Westdahl Peak, located on a gently sloping plateau that may represent the surface of a truncated ancestral cone of Pleistocene age or older [*Miller et al.*, 1998]. Documented eruptions at or near Westdahl Peak occurred in 1795, 1796, 1820, and 1827–1830, but during that time period other eruptions might have gone undetected, given the volcano's remote location [*Miller et al.*, 1998]. Westdahl was frequently active during the latter half of the twentieth century, with documented eruptions in 1964–1965, 1978–1979, and 1991–1992 (Figure 1b). The volcanic explosivity index of these last three eruptions was two or three, which corresponds to a "moderate" or "moderate-large" explosive event with 10^6–10^8 m^3 of erupted products [*Newhall and Self*, 1982; *Simkin and Siebert*, 1994, p. 115].

[11] In March–April 1964, a fissure eruption produced lava flows on the east flank of Westdahl Peak [*Wood and Kienle*, 1990]. A vulcanian eruption through glacier ice in 1978 produced a crater with a diameter of 1.5 km and depth of 0.5 km near the 1964 vent (Figure 1). The eruption column reached a height of 10 km, and an ash deposit of 18 cm thickness was observed 15 km southwest of the vent. The eruption also produced a lahar down the southwest flank of Westdahl Peak that reached the sea [*Global Volcanism Network*, 1978].

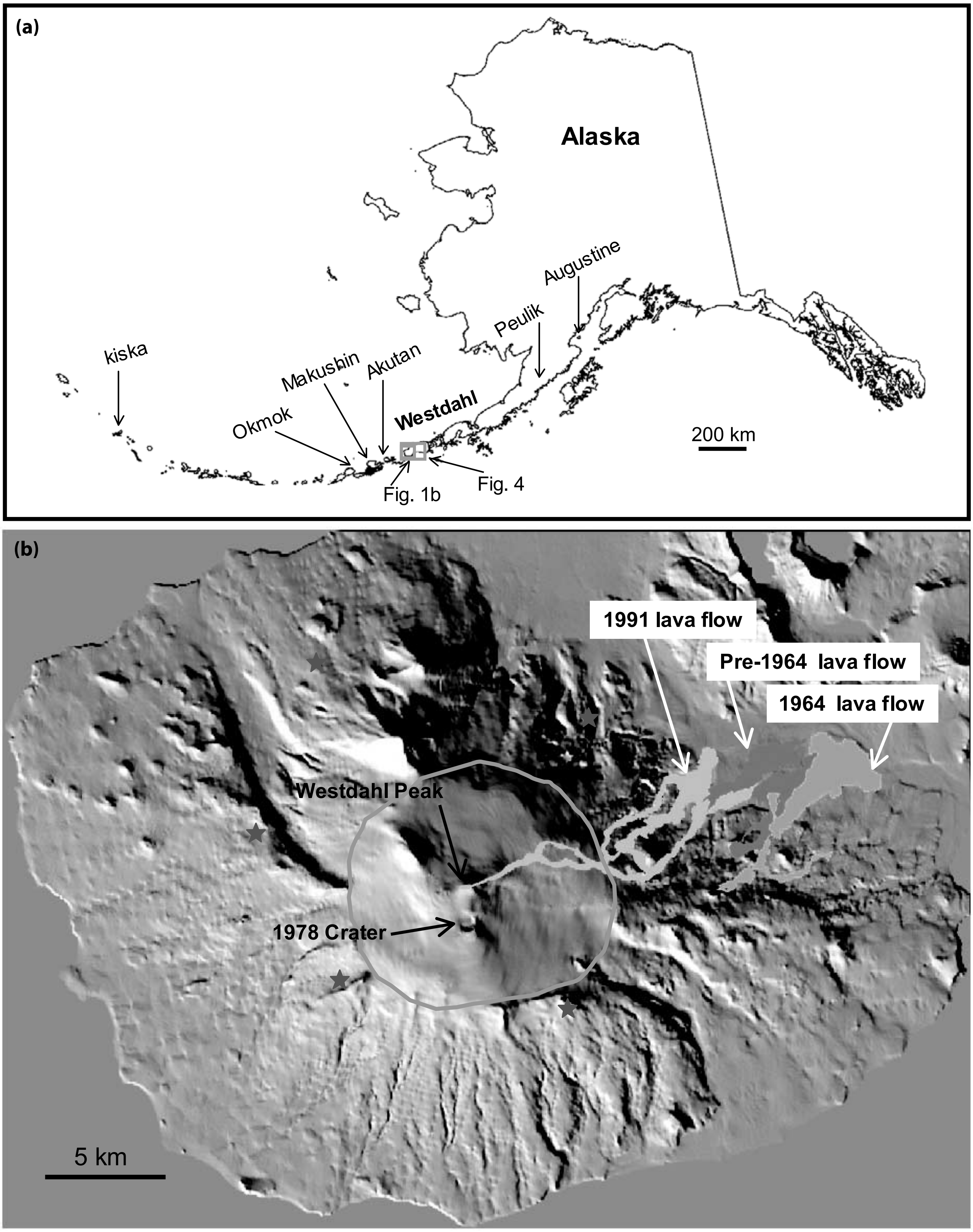

Figure 1. (a) Map of Alaska including the 2500-km long Aleutian volcanic arc. Rectangles outline areas are shown in Figures 1b and 4. (b) Shaded-relief image of Westdahl volcano. The 1978 crater, the Westdahl Peak (1991–1992 eruption vent), and the lava flows from pre-1964, 1964, and 1991 eruptions are labeled. Stars denote locations of seismic stations near the volcano. The glacier on the volcano is outlined in orange. See color version of this figure at back of this issue.

Table 1. SAR Images Used for This Study[a]

Date 1, YMD	Orbit 1	Date 2, YMD	Orbit 2	Track	h_a, m	RMSE[b] (10^{-3} m)	RMSE[c] (10^{-3} m)	RMSE[d] (10^{-3} m)	Figure
910907	E1/00757	911025	E1/01445	15	50				2a
910910	E1/00800	911028	E1/01488	15	−205				2b
911028	E1/01488	911112	E1/01703	15	55				2c
911013	E1/01273	911121	E1/01832	15	51				2d
911121	E1/01832	911130	E1/01961	15	−455	3.10	3.23	3.75	2e, 2f
920119	E1/02670	920125	E1/02756	36	123				2g
920131	E1/02842	920206	E1/02928	36	−225				2h
920604	E1/04640	930902	E1/11153	487	−1490	4.58	5.05	5.20	3a, 5a
920712	E1/05184	930627	E1/10194	29	455	2.49	2.52	3.09	3b, 5b
920920	E1/06186	930905	E1/11196	29	148	2.34	2.51	2.55	3c, 5c
921011	E1/06415	930926	E1/11415	322	−150	2.70	2.72	2.75	3d, 5d
930902	E1/11153	950826	E1/21517	487	387	4.12	4.41	4.70	3e, 5e
930921	E1/11425	951019	E1/22290	258	79	2.70	2.80	2.88	3f, 5f
931007	E1/11654	950806	E1/21517	487	−316	4.32	4.45	4.50	3g, 5g
931007	E1/11654	960811	E2/06854	487	497	4.53	4.60	4.68	3h, 5h
951009	E1/22290	981009	E2/18148	258	−67	3.26	3.55	3.68	3i, 5i
971015	E2/12866	990801	E2/22385	487	141	3.17	3.17	3.26	3j, 5j
970611	E2/11198	000913	E2/28232	322	238	3.89	3.87	3.94	3k, 5k
990804	E2/22428	000823	E2/27939	29	341	1.68	1.76	1.83	3l, 5l
921011	E1/06479	970611	E2/11198	322	−714	4.18	4.33	4.65	3m, 5m
930921	E1/11425	981009	E2/18148	258	−408	3.49	4.43	4.57	3n, 5n
921006	E1/06415	981009	E2/18148	258	−177	5.10	5.35	5.52	3o, 5o

[a] Dates are image acquisition times in YMD (year, month, day; read 910907 as September 7, 1991) format. Orbit numbers include the satellite ID (E1, ERS1, E2, ERS2) and orbit on which the images were acquired. The same track number applies to both images in an interferometric pair.

[b] RMSE between the observed and modeled interferograms and seven unknowns for each model (x_1', x_2', x_3', ΔV, and three ramping-phase parameters) was optimized.

[c] This is a case where the horizontal position of the deformation source was fixed using the weighted average of locations from the posteruption interferograms and only five model parameters were optimized.

[d] In this case the model source in three dimensions was fixed and only four parameters were optimized.

[12] Pilots reported the beginning of a fissure eruption through ice at Westdahl at 0200 UT on 30 November 1991. The fissure extended from near the summit of Westdahl Peak eastward for about 8 km. Ash venting occurred discontinuously along most of the fissure. Dramatic lava fountaining was observed along the lower portion of the fissure, feeding several streams of lava that descended on the east flank (Figure 1b). Fountaining and phreatic activity produced ash plumes that rose to an altitude of 7 km, prompting the U.S. Federal Aviation Agency to divert air traffic. Activity declined in mid-December 1991 and ceased by mid-January 1992 [*Miller et al.*, 1998].

2. InSAR Observations of Ground Deformation

[13] We obtained all of the archived ERS-1 and ERS-2 images that are suitable for measuring surface deformation at Westdahl. Technical problems with ERS-2 preclude using its 2001 images of Westdahl for this purpose, so the useful data set spans the period from 1991 to 2000. Originally, we processed the radar data together with a U.S. Geological Survey (USGS) DEM with a horizontal resolution of 60 m and a root mean square vertical error of 15 m [*Gesch*, 1994], using the two-pass InSAR method described by *Massonnet and Feigl* [1998]. A new DEM from the Shuttle Radar Topography Mission (SRTM) became available (http://edc.usgs.gov/products/elevation.html) in December 2002. We then used the 1-arc second (about 30 m) SRTM DEM, which has a relative vertical height accuracy of better than 10 m [*Farr and Kobrick*, 2000; NIMA Fact Sheet at http://164.214.2.59:80/srtm/factsheet.html], to reprocess the interferograms. We produced 22 interferograms with relatively good coherence over the area of interest (Table 1).

[14] The interferograms listed in Table 1 were produced with SAR images acquired in six different imaging modes (Tables 1 and 2). Tracks 15, 29, 258, and 487 are descending passes in which the ERS satellites travel from about N13°E to S13°W. In this mode, the SAR sensors are directed ~N77°W with look angles of 20°–25.5° from the vertical over the center of the volcano. Tracks 36 and 322 are ascending passes in which the satellites travel from about S13°E to N13°W with look angles of 22.7° and 20.9°, respectively. The line of sight (LOS) vectors for SAR images, defined as [east, north, up], are shown in Table 2. Among the Westdahl interferograms described in this paper (Table 1 and Figures 2 and 3), 5 have altitudes of ambiguity, h_a, ranging from 50 to 79 m, and 17 have values of h_a larger than 123 m. For an InSAR image with h_a of 50–79 m, removing the topographic contribution from the original interferogram with a DEM of 10-m systematic vertical error causes a phase error of 0.2–0.1 of a fringe [e.g., *Massonnet and Feigl*, 1998]. Therefore any artifacts in the interferograms (Figures 2 and 3) due to possible errors in the DEM are negligible.

[15] Inspection of the Westdahl interferograms, which span time periods that range from several days during the arctic winter to a few years between summers, leads to the

Table 2. LOS Vectors for Six Different Satellite Tracks Listed in Table 1

Track	LOS Vector (East, North, Up)
15	(0.326, −0.078, 0.942)
36	(−0.375, −0.091, 0.922)
29	(0.331, −0.079, 0.940)
258	(0.375, −0.090, 0.923)
322	(−0.347, −0.083, 0.934)
487	(0.423, −0.101, 0.900)

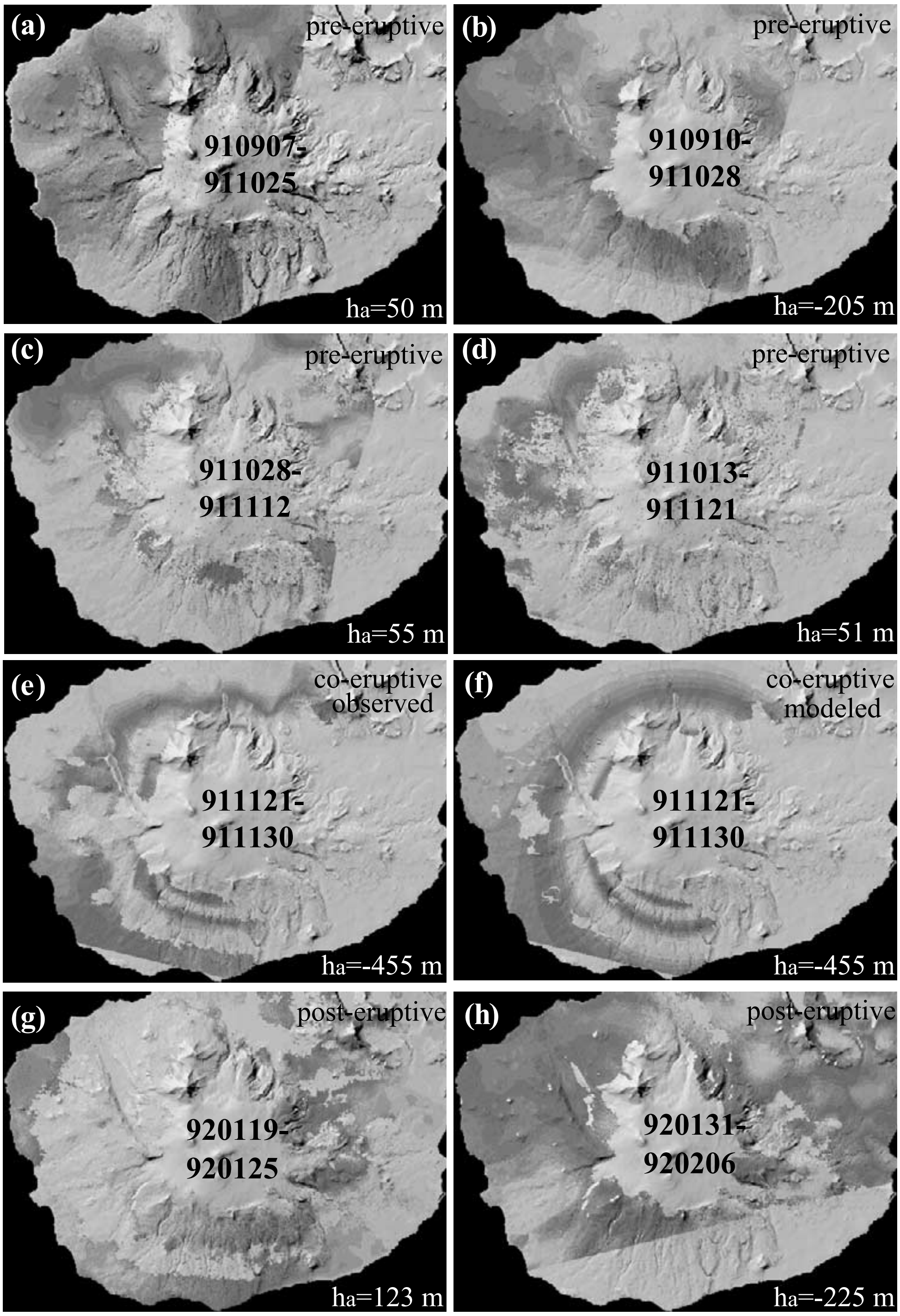

Figure 2. Observed (a–e, g, h) and modeled (f) interferograms for time periods soon before (Figures 2a–2d), including (Figures 2e, 2f), and after (Figures 2g, 2h) the start of an eruption on 29 November 1991. Topographic effects have been removed using a DEM. Each fringe (full color cycle) represents 2.83 cm of range change between the ground and the satellite. Additional information on SAR images used for the interferograms is given in Table 1. Each interferogram covers the same area as Figure 1b. The altitude of ambiguity, h_a, for each interferogram is labeled. Figures 2e and 2f show observed and modeled deflation, respectively, during the first 20 hours of the eruption. Areas that lack interferometric coherence are uncolored. See color version of this figure at back of this issue.

following conclusions concerning the persistence of C-band radar interferometric coherence: (1) coherence is maintained for up to 6 years if the images are acquired during summer to late fall, except on the ice-covered upper slopes of the Westdahl edifice (Figure 3); (2) the coherent area for interferograms with a longer time window is not significantly smaller than that for a shorter window (Figures 2 and 3); (3) in areas of permanent ice, radar coherence is lost in a

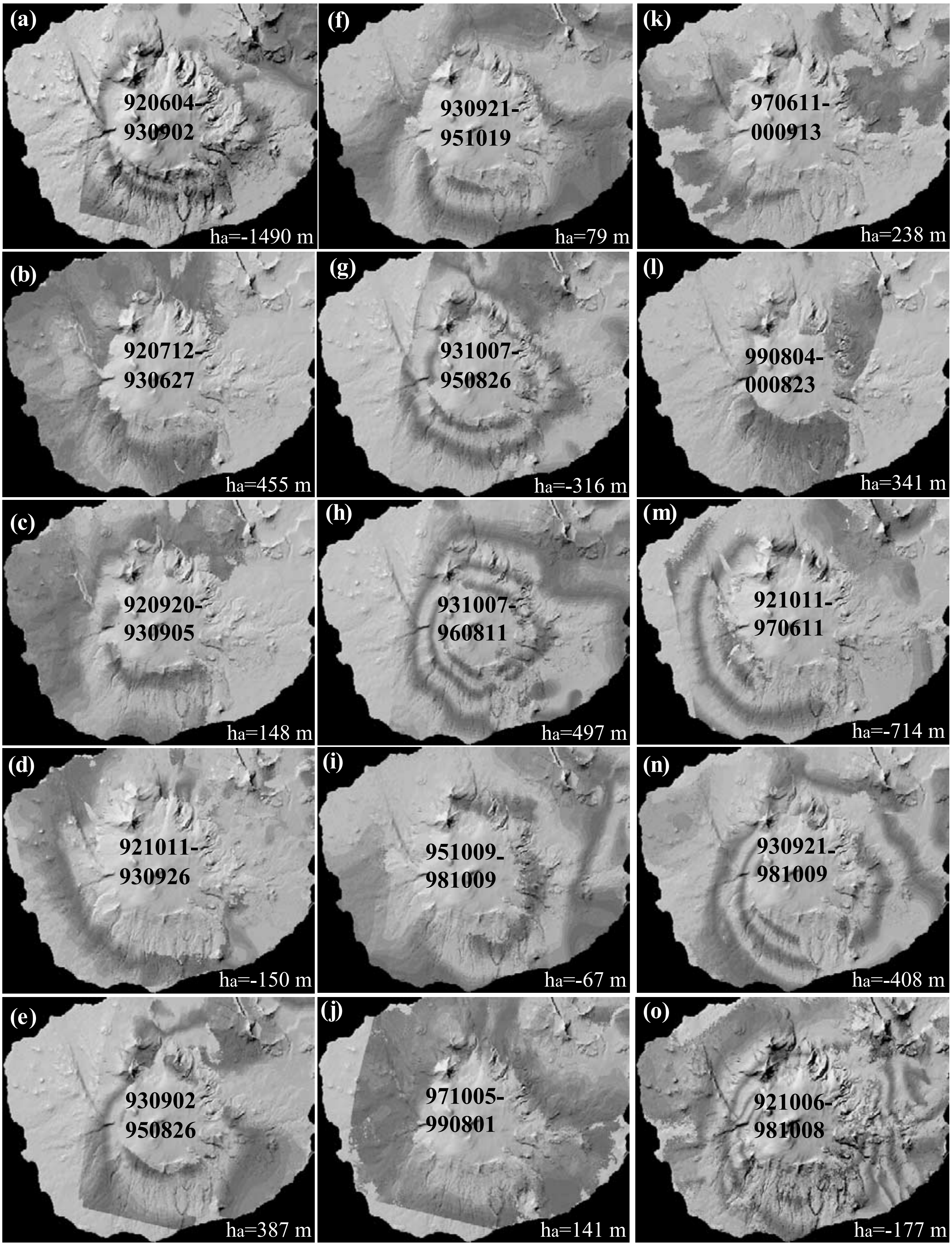

Figure 3. Observed interferograms for various time windows during 1991–2000 starting after the 1991–1992 eruption and showing progressive inflation. Each fringe (full color cycle) represents 2.83 cm of range change between the ground and the satellite. Additional information on SAR images used for the interferograms is given in Table 1. Each interferogram covers the same area as Figure 1b. The altitude of ambiguity, h_a, for each interferogram is labeled. Areas that lack interferometric coherence are uncolored. See color version of this figure at back of this issue.

matter of days or less (Figure 2); (4) coherence is sometimes maintained for a few days even during the winter when the volcano's flanks are blanketed by snow (Figure 2); and (5) coherence is worst on the southeast flank, suggesting the presence of relatively loose material, relatively dense vegetation cover, or other environmental factors that promote coherence loss.

[16] Interferograms for periods before, during, and after the 1991–1992 eruption are shown in Figure 2. Figures 2a–2d collectively bracket a time window of about 75 days that ended less than 8 days before the start of the eruption. Figures 2g–2h span a time interval of about 12 days after the end of the eruption. About half of a fringe over the northwestern flank of the volcano can be seen in the interferogram from 7 September to 25 October 1991 (Figure 2a). However, such a phase change was absent from an interferogram spanning a similar time interval from 10 September to 28 October 1991 (Figure 2b), suggesting that the phase change in Figure 2a was probably caused by atmospheric anomalies. None of these interferograms includes more than one recognizable fringe (i.e., 2.83 cm of range change in the LOS direction) and no consistent fringe pattern is discernible, so any ground deformation that might have occurred during this period was too small to measure. Alternatively, deformation from a very shallow source might have been localized near the summit, where coherence is lacking, and escaped detection.

[17] Two fringes are visible on Westdahl's north, west, and south flanks in Figure 2e, indicating displacement of the upper part of the volcano by more than 5.7 cm. The progression of colors from red to yellow to blue toward the summit represents an increase in the LOS distance from the satellite to the ground surface, which corresponds to subsidence of the surface. The images used for this interferogram were acquired at about 2200 UT on 21 and 30 November 1991. Subsidence was probably caused by magma withdrawal during the first day of the eruption, which started at 0200 UT on 30 November 1991. The largest displacements might be expected near the summit, but this area is covered by snow and ice and does not maintain coherence. Nonetheless, the total amount of subsidence can be estimated by modeling the partial deformation field revealed by the interferogram.

[18] Figures 3a–3o include 15 interferograms that collectively span the time from summer 1992 to summer 2000 and show progressive inflation of Westdahl following its 1991–1992 eruption. Inspection suggests that the inflation rate decreased with time. For example, the 1992–1993 interferograms (Figures 3a–3d) each show about one fringe, whereas the 1993–1995 interferograms show about one and a half fringes (Figures 3e–3g). Moreover, the 1997–1999 interferogram (Figure 3i) shows fewer fringes than the 1993–1995 interferograms (Figures 3e–3g), and the 1999–2000 interferogram (Figure 3l) shows fewer fringes than the 1992–1993 interferograms (Figures 3a–3d).

[19] Several of the interferograms, (e.g., Figures 3e and 3i) seem to be contaminated by atmospheric delay anomalies, which can be severe in the Aleutian environment [*Lu et al.*, 2000a]. Inspection of a larger area in the same two interferograms (Figure 4) reveals probable atmospheric anomalies amounting to a few fringes. Figure 4a, which is a larger version of Figure 3e, shows a few fringes on the north flank of Shishaldin volcano, about 26 km northeast of Westdahl. We have studied other interferograms of Shishaldin [*Lu et al.*, 2003b] and discovered no consistent pattern of ground deformation, so the fringes in Figure 4a probably represent an atmospheric anomaly. Similarly, Figure 4b is a larger version of Figure 3i and shows a fringe pattern at Shishaldin and elsewhere east of Westdahl that we attribute to atmospheric delay anomalies rather than to deformation. Note that the atmospheric anomalies are not always correlated with the topography. For example, the anomaly over Shishaldin volcano in Figure 4a is present on the northern flank but not on the southern flank of the volcano. Similarly, the anomaly on the eastern flank of Westdahl volcano is not present on the western flank. The fringe over Fisher volcano represents a long-term subsidence and has been confirmed from many other interferograms that are not shown in this paper.

3. InSAR Deformation Modeling

[20] Our goal is to characterize the inflation rate of Westdahl as a function of time on the basis of interferograms for 16 different, partly overlapping epochs that span 9 years, including coeruptive and posteruptive periods (Table 1 and Figures 2e and 3). On the basis of the radial pattern of the displacement field, we assume that deformation is caused by a volume change in a spherical magma reservoir and model the surface displacement field using a tensile spherical source within a homogenous elastic half-space [*McCann and Wilts*, 1951]. This formulation is more general but otherwise equivalent to that of *Mogi* [1958], which is commonly cited in the volcanological literature. Mogi used a value of 0.25 for Poisson's ratio, ν, whereas *McCann and Wilts* [1951] retained the functional dependence of surface displacement on ν. The result of Mogi is exactly recoverable from our equations (1) and (2) for $\nu = 0.25$.

[21] We specify a Cartesian coordinate system with the east, north, and up axes having an origin collocated with the upper, left (northwest) corner of the interferograms. The predicted displacement (u) at the free surface of an elastic homogeneous half-space due to a change in the volume (ΔV) of a sphere (i.e., a presumed magma reservoir) is:

$$u_i(x_1, x_2, x_3 = 0) = \beta \frac{x_i - x_i'}{R^3} \Delta V, \tag{1}$$

where x_1', x_2', and x_3' are the horizontal locations and depth of the center of the sphere, R is the distance between the sphere and the location of observation (x_1, x_2, and 0), and β is a constant dependent on Poisson's ratio, ν, of the host rock given by

$$\beta = \frac{(1-\nu)(1+\nu)}{2\pi(1-2\nu)}. \tag{2}$$

[22] For each of the interferograms (Figures 2e and 3), we determined best fitting parameters for the location and volume change of the source. We introduced linear terms in our model to account for any phase ramp due to satellite position errors, which might not be completely removed during interferogram processing [*Massonnet and Feigl*, 1998]. To account for topographic effects, we adopted a simple method proposed by *Williams and Wadge* [1998], in

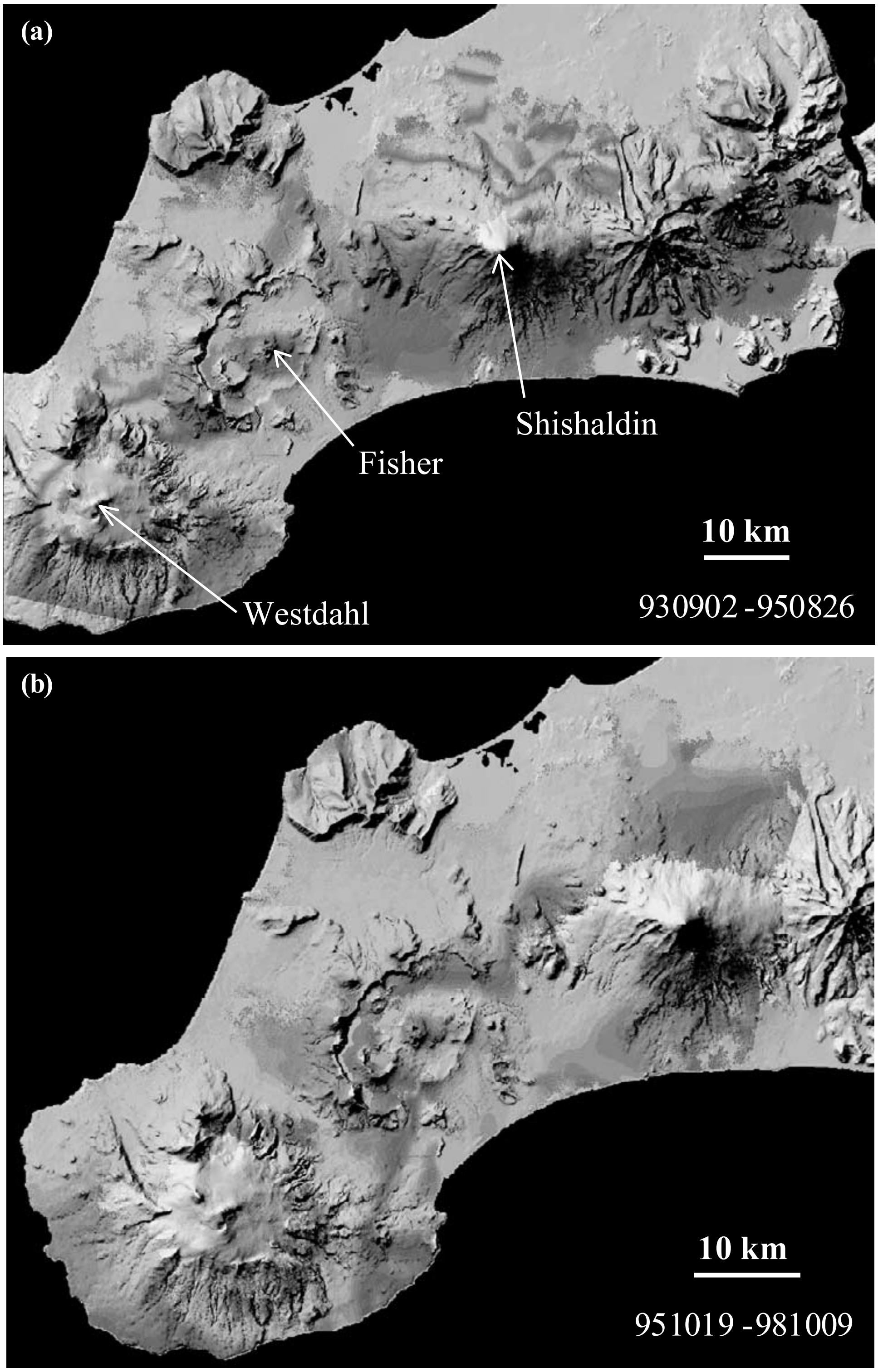

Figure 4. Observed interferograms of the western part of Unimak Island showing the effects of atmospheric delay anomalies (see text). (a) This image was produced from the same SAR images used for Figure 3e, but this version covers a larger area. (b) Same as Figure 3i, but a larger area. One fringe (a full color cycle) represents the range change of 2.83 cm. Outlines of these two images are shown in Figure 1a. Peaks of Westdahl (elevation of ~1550 m), Fisher (elevation of ~500 m), and Shishaldin (elevation of ~2800 m) are labeled in Figure 4a. See color version of this figure at back of this issue.

which the elevation of the reference surface varies according to the elevation of each computation point in the model. There are seven unknowns for each model (x_1', x_2', x_3', ΔV, and three ramping-phase parameters). We used the downhill simplex method and Monte Carlo simulations [*Press et al.*, 1992] to estimate optimal parameters and uncertainties and the root mean square error (RMSE) between the observed and modeled interferograms as the prediction-fit criterion.

[23] During the parameter optimization for each InSAR image (Figures 2e and 3), we did not model the tropospheric effects, as did *Beauducel et al.* [2000], for several reasons. First, because the topographic relief over the deformation area is less than 900 m, the topography-correlated tropospheric fringes should be insignificant [*Beauducel et al.*, 2000; *Wicks et al.*, 2002]. Second, as shown in Figure 4, the severe atmospheric anomalies are not always correlated with topography. Third, the topography-correlated atmospheric noise could vary in amplitude at different times. Because we do not have any constraints on atmospheric conditions (water vapor content, pressure, and temperature) over the study area, calculating the topography-correlated atmospheric anomalies with the standard tropospheric model is subject to large uncertainties. Fourth, topography-related atmospheric artifacts could be either positive or negative, depending on the relative changes in water vapor profiles. Therefore if many interferograms (15 InSAR images in our case) are used to construct the deformation model, the effects of artifacts should partly cancel, and the model should be relatively free of atmospheric effects.

[24] Based on equation (2), the Poisson's ratio ν used in deformation models should be chosen with care. *Christensen* [1996] determined the value of ν for numerous rock types from measurements of compressional and shear wave velocities and showed that the average ν for basalt is 0.30. Therefore we chose $\nu = 0.30$ for our analysis. We tested the sensitivity of ν to both the estimated volume change and depth of the source. A decrease in ν from 0.30 to 0.25 can result in an increase of $\sim$20% in estimated volume change, and an increase in ν from 0.30 to 0.35 can result in a decrease of $\sim$20% in estimated volume change. We found that the depth of the source is not affected by the choice of ν, because the depth is included in the parameter R (equation (1)).

[25] The volume change of the spherical source derived from deformation data also depends on the compressibility of magma in the reservoir [*Johnson et al.*, 2000]. For example, adding a given volume of magma to a relatively small, relatively gas-poor (i.e., incompressible) reservoir would produce a larger pressure change and therefore a larger surface volume change than adding the same volume to a larger, gas-rich reservoir, especially if an exsolved gas phase is present. We ignored this effect in our model, because there are no useful constraints on the volume of stored magma or its gas content for Westdahl volcano. For incompressible magma and $\nu = 0.3$ for the volcanic edifice, the $\Delta V_{\mathrm{edifice}}/\Delta V_{\mathrm{magma}}$ ratio is 1.4, where $\Delta V_{\mathrm{edifice}}$ is the volume of ground surface uplift and $\Delta V_{\mathrm{magma}}$ is the volume of magma intruded into the magma reservoir [*Johnson et al.*, 2000]. The presence of exsolved gas lowers the ratio of $\Delta V_{\mathrm{edifice}}/\Delta V_{\mathrm{magma}}$, and therefore increases the estimated magma volume change. This means that our calculation most likely underestimates actual magma volume change in the reservoir.

[26] The interferograms in Figures 2e and 3 were first modeled individually. Figures 2f and 5 show the corresponding modeled interferograms calculated using the best fitting parameters for each interferogram. The horizontal locations of the best fitting models are shown in Figure 6a. The semiaxes of the ellipsoids represent the uncertainties of locations at one standard deviation (1σ). The value of RMSE is generally less than 5 mm (Table 1). The modeled source locations are clustered near Westdahl Peak and do not migrate significantly with time or space during 1991–2000 (Figure 6a). Therefore our modeling shows that the inflation source is unlikely to have moved laterally from 1992 to 2000, and this is presumably the same source that deflated during the 1991–1992 eruption (Figure 6a).

[27] Next, we fixed the horizontal position of the deformation source using the weighted average of locations from the posteruption interferograms. This reduced the number of modeled parameters from seven to five for each interferogram. We then reestimated the remaining parameters, subject to the fixed horizontal position constraint. The resulting best fit source depths, volume changes, and uncertainties are shown in Figure 6b. The error bars and circles represent the uncertainty bounds for depth and volume change at 1σ, respectively. The RMSE value for each InSAR image is shown in Table 1. Fixing the horizontal position increases the RMSE by only about 0.2 mm (Table 1), suggesting that the inflation source did not move laterally from 1992 to 2000. The average source depth is 5.8 km below sea level (7.3 km beneath Westdahl Peak). Two of the modeled source depths that deviate from this average are probably affected by atmospheric delay anomalies. The two greatest depths ($\sim$8 and $\sim$10 km) were estimated from the interferograms in Figures 3e and 3i, which show evidence of atmospheric contamination. The model depth for the 1999–2000 interferogram (Figure 3l) is also deeper than the average (Figure 6b). The amount of deformation suggested by the 1999–2000 image is the least among all of the 16 interferograms; therefore the estimated model parameters are more susceptible to atmospheric contamination. Taken in total, the results shown in Figures 6a and 6b lead us to conclude that the sources of coeruptive deflation and posteruptive inflation were the same, and they remained essentially stationary during the 9-year period of study.

[28] Finally, we fixed the model source in three dimensions (horizontal position and depth) using a weighted average of the 15 model locations during the posteruption periods. This reduced the number of modeled parameters from seven to four for each interferogram. With a fixed source location, equation (1) is linearized, so we calculated linear least squares inversions [e.g., *Menke*, 1989] to reestimate the volume changes for each interferogram (Figure 6c). We found that the average increase in RMSE value is about 0.4 mm (Table 1). The small increase in RMSE validates our conclusion that the inflation source did not move during 1992 and 2000.

[29] Inspection of Figure 6c suggests that the rate of volume change was not constant with time. In other words, ΔV_j is not solely dependent on the duration of epoch j. Volume changes soon after the 1991–1992 eruption appear to be greater than those at later times. We tested this hypothesis by fitting a linear function to the estimated volume changes for the 15 posteruption epochs, weighted

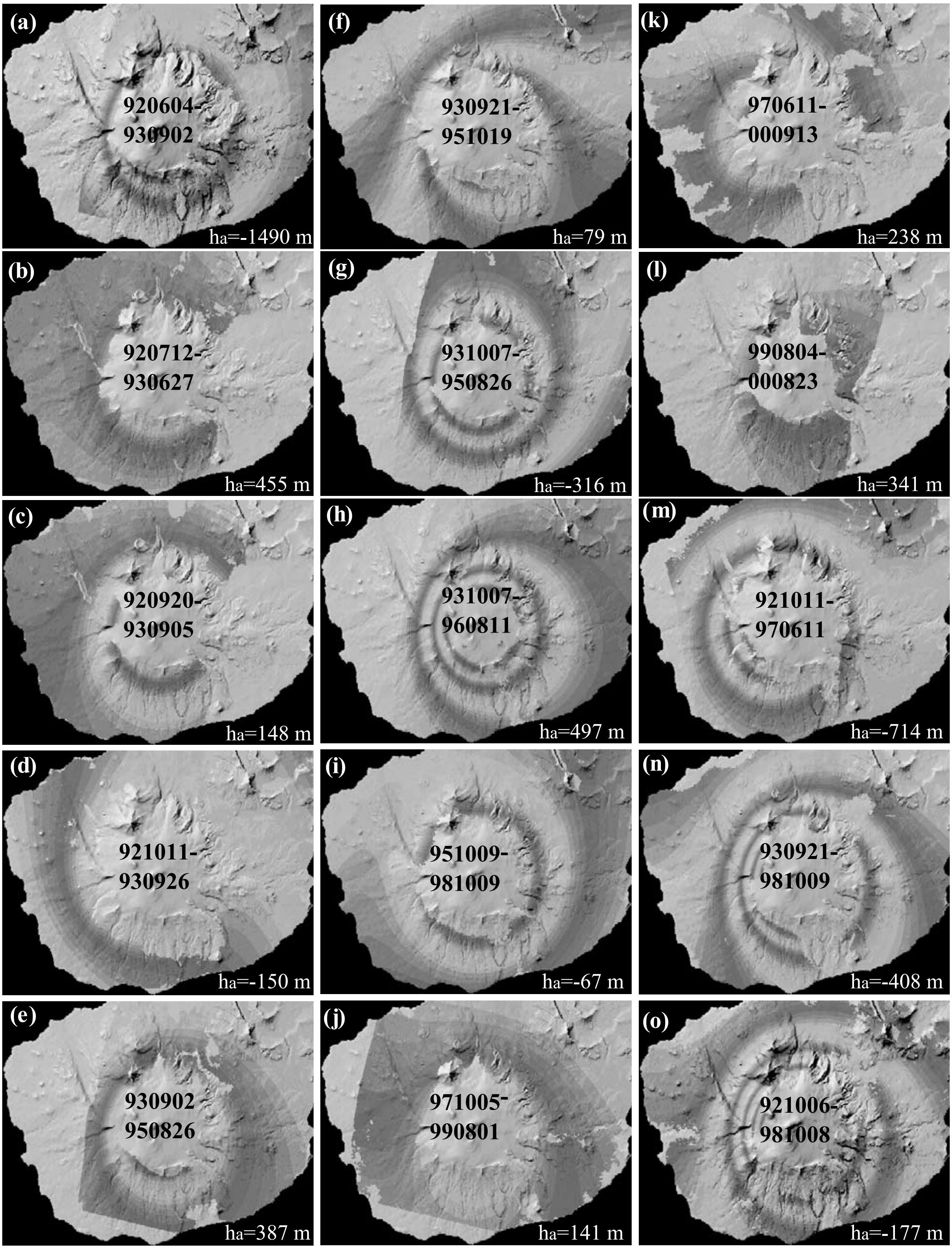

Figure 5. Modeled interferograms that correspond to the observed images in Figure 3. These synthetic interferograms were produced using the corresponding best fit sources from a model described in the text. Each fringe (full color cycle) represents 2.83 cm of range change between the ground and the satellite. The altitude of ambiguity, h_a, for each interferogram is labeled. Areas that lack interferometric coherence are uncolored. See color version of this figure at back of this issue.

with the appropriate uncertainties. The choice of a linear function reflects an assumption that the volume changes were due to a constant flux (Q) of magma into the reservoir

$$\Delta V_j = \left(t_{j1} - t_{j0}\right)Q, \tag{3}$$

where t_{j0} and t_{j1} are the times at the beginning and end, respectively, of epoch j. Results of this analysis are shown in Figure 7a. A constant magma flux does not fit the modeled volume changes particularly well; it underestimates the changes for early epochs and overestimates them for later epochs. A linear regression of the residuals (lower curve in Figure 7a) confirms that this systematic trend in prediction mismatch is significant at the 99% confidence level [e.g., *Davis*, 1973], indicating that the constant flux model is inadequate.

[30] We appealed to a fluid flow model in which magma reservoir deformation is the result of magma flowing into the reservoir owing to a pressure gradient between the reservoir and a deeper source by means of a conduit. For the case of flow through a cylindrical pipe from a constant pressure source [e.g., *Dvorak and Okamura*, 1987]

$$Q = Q_0\, e^{-kt}, \tag{4}$$

where Q_0 is the initial magma flux into the reservoir at $t = 0^+$. The parameter k is a function of the frictional loss factor, magma viscosity, steady state (equilibrium) change in magma reservoir volume, and length and radius of the conduit [*Dvorak and Okamura*, 1987]. We treated k as a single parameter and did not attempt to estimate the separate flow parameters.

[31] The time-dependent change in volume during epoch j is obtained by integrating equation (4):

$$\Delta V_j = -\left(e^{-kt_{j1}} - e^{-kt_{j0}}\right)Q_0 k/\beta, \tag{5}$$

where β is a constant defined in equation (2). We fit equation (5) to the 15 volume changes modeled from posteruption interferograms (Figure 6c). By minimizing a merit function defined as the chi-square difference between the estimated volume changes and the predicted ones based on equation (5), we solved for Q_0 while sweeping through k parameter space. The best fit solution was found at $k = 0.17$ per year and $Q_0 = 9.2 \times 10^6$ m^3/yr. The time constant, i.e., $1/k$, for inflation is about 6 years. A linear regression of the residuals from the exponential decay model indicates no significant trend (lower curve of Figure 7b). Hence this is our preferred model for the magma flux as a function of time. The subsurface volume change calculated from our model for 1998–2001 is about 3.0×10^6 m^3/yr, which is similar to that estimated based on GPS data only (4.9×10^6–10.0×10^6 m^3/yr) [*Mann and Freymueller*, 2003].

4. Discussion

4.1. Magma Accumulation Since 1991–1992 Compared With the Volumes of Recent Lava Flows

[32] In the simplest case, the volume of magma added to a reservoir between eruptions is directly related to the volume of magma erupted. With this in mind, we compared the magma volume change estimated from our model with the volumes of recent lava flows at Westdahl. The 1991–1992 flow was estimated from an oblique aerial photograph to be about 7 km long, up to 3 km wide, and 5–10 m thick, with an area of about 5 km^2 and volume of 0.025–0.050 km^3 (T. Neal, personal communication, 2002). These estimates have since been refined using SAR imagery. Over gently sloping terrain, the SAR backscattering signal is primarily controlled by surface roughness. Surfaces that are rough at scales comparable to or larger than the radar wavelength have large radar cross sections and appear bright in SAR images. The rough aa texture of the 1991–1992 lava flow makes it a radar-bright feature. *Rowland et al.* [1994] used an SAR image acquired on 27 February 1992 to estimate the area of the 1991–1992 flow to be 6.3 km^2, which corresponds to a volume of 0.03–0.06 km^3, assuming an average thickness of 5–10 m.

[33] *Dean et al.* [2002] used multiple SAR images to map the 1991–1992, 1964, and pre-1964 lava flows. All of the flows have similar radar cross sections, so differentiating them on the basis of SAR imagery alone is partly subjective. Dean et al. estimated the area of the 1991–1992 flow to be 3.79 km^2, but Z. Lu et al. (manuscript in preparation, 2003; hereinafter referred to as Z. Lu et al., manuscript in preparation, 2003) concluded that part of the 1991–1992 flow was mistaken for pre-1964 lava and therefore this estimate is too small. Lu et al. refined the area estimates for all three flows using multiple SAR images acquired shortly after the 1991–1992 eruption as well as an optical Landsat 7 image acquired on 27 September 2000. They used SAR images to map the eruptive fissures and nonvegetated upper parts of the flows and the Landsat image to differentiate the lower parts, which are vegetated to different degrees. The resulting estimates are 7.28, 9.20, and 8.35 km^2 for the pre-1964, 1964, and 1991–1992 flows, respectively. The 1964 estimate is similar to that by *Dean et al.* [2002] (9.20 versus 9.86 km^2), but the 1991–1992 estimate is considerably larger (8.35 versus 3.79 km^2), for the reason given above. The areas and presumably the volumes of all three flows are similar; i.e., the areas differ by less than 10%, and the average thicknesses probably differ by less than a factor of two.

[34] The volume of lava at the surface differs from the corresponding volume of magma at depth mainly as a result of vesiculation. As magma rises toward the surface, the resulting decrease in confining pressure causes gases to exsolve into bubbles. Some of the bubbles remain trapped as vesicles in the erupted products, contributing to their volume. For near-vent basaltic lavas, the bulking factor from vesiculation can be greater than a factor of two. For example, *Mangan et al.* [1993] showed that the average vesicularity of vent lavas from the Puu Oo-Kupaianaha eruption at Kilauea is 66%, very close to the predicted value of 69% that is based on the melt composition and equilibrium gas content. On the other hand, surface degassing of active lava flows reduces their vesicularity and hence their volume. *Cashman et al.* [1994] showed that the vesicularity of the same Puu Oo-Kupaianaha lavas decreased progressively to 10–20% at distances of 10–12 km from the vent. On this basis, we assumed an average vesicularity of 15% for the 1964 and 1991–1992 lava flows at Westdahl and adjusted their volumes accordingly.

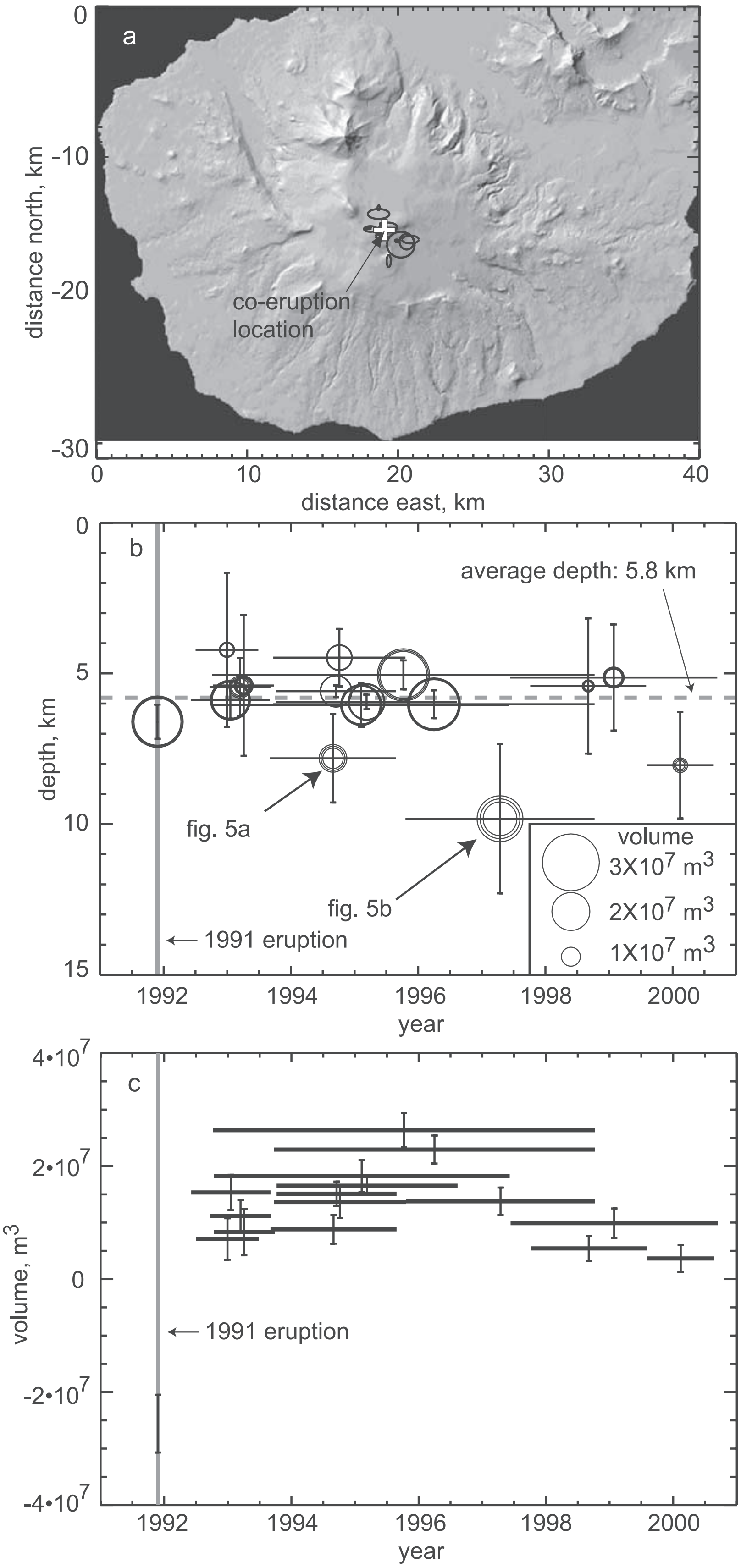

a
0
-10
-20
-30
distance north, km
co-eruption location
0
10
20
30
40
distance east, km
b
average depth: 5.8 km
depth, km
0
5
10
15
fig. 5a
fig. 5b
volume
3X10^7 m^3
2X10^7 m^3
1X10^7 m^3
← 1991 eruption
1992
1994
1996
1998
2000
year
c
4•10^7
2•10^7
0
-2•10^7
-4•10^7
volume, m^3
← 1991 eruption
1992
1994
1996
1998
2000
year

[35] On the basis of the area estimates of Z. Lu et al. (manuscript in preparation, 2003) and assuming an average thickness of 5–10 m for the 1964 and 1991–1992 flows, the flow volumes range from 4.2 × 10^7 to 9.2 × 10^7 m^3. Reduced by 15% to account for vesicularity, the subsurface volume ranges from 3.6 × 10^7 to 8.0 × 10^7 m^3 (Figure 7c). The steady state volume change of the magma reservoir from our model is 5.4 ± 0.6 × 10^7 m^3, which compares favorably with our volume estimates for the vesicle-free 1964 and 1991–1992 lava flows (Figure 7c). This ignores the effect of magma-reservoir compressibility, which would increase our estimate of the steady-steady volume change by some amount that is unknown but probably smaller than the factor of two uncertainty in flow volumes. So it seems that recent activity at Westdahl has followed a somewhat repeatable pattern in which the magma flux decays exponentially with time but nonetheless causes a reservoir to rupture when some threshold is crossed. The volume of the resulting intrusion or eruption approximates the volume added to the reservoir since the start of the inflation cycle, which then begins anew. The factor of two uncertainty in the average lava flow thickness and therefore in the flow volume estimates admittedly leaves room for a different conclusion, i.e., that lava production during the past three eruptions could have varied by that amount, and the apparent regularity in the eruption cycle could be illusory or coincidental. The weight of available evidence, in our opinion, favors the first interpretation.

4.2. Dynamics of Reservoir Deflation and a Model for the Eruption Cycle

[36] We have shown that Westdahl's inflation rate decayed exponentially with time following its 1991–1992 eruption, but how did the deflation rate evolve as the eruption progressed? The eruption lasted for about 45 days, including 5 days of strong lava extrusion from 29 November to 4 December 1991 [*Global Volcanism Network*, 1991]. Using an interferogram that spans 21–30 November 1991, including the first 20 hours of the eruption, we estimated the depth of the deflation source to be 6.6 km below sea level (Figures 2e, 2f, and 6b). This is slightly deeper than the average depth of the inflation source determined from 15 posteruption interferograms (5.8 km), but the difference is not significant at 1σ. The horizontal locations of the deflation and inflation sources are also similar (Figure 6a), so we concluded that the two sources are the same. The volume change of the reservoir during the first 20 hours of the eruption, based on a model of the coeruptive interferogram, was 2.5 × 10^7 m^3. This is 46% of the steady state volume change of the reservoir. In other words, nearly half of the total volume that could have been added to the reservoir between eruptions was lost during the first day of the eruption. The same deflation volume, adjusted for 15% vesicularity, corresponds to 2.9 × 10^7 m^3 of erupted lava. This is about 35% of the total volume erupted during the 1991–1992 eruption, based on our estimate. If nearly one half of the total reservoir deflation occurred during the first day of an eruption that lasted about 45 days, the deflation rate must have decreased markedly with time. We assumed that deflation (1) slowed exponentially according to equation (4) and (2) was 46% complete in 20 hours based on the coeruptive interferogram. The resulting deflationary decay constant, *k*, is ~0.8 per day. This is in accordance with field observations that the vigor of the eruption declined markedly after the first 5 days and that the flows had stopped advancing by 3 December 1991 [*Global Volcanism Network*, 1991]. Exponentially decreasing deflation rates also have been observed during eruptions at other basaltic shield volcanoes, including Kilauea [*Dvorak and Okamura*, 1987], Mauna Loa [*Lockwood et al.*, 1987], and Krafla [*Tryggvason*, 1980]. Estimated values of *k* range from 0.8 per day for Krafla [*Tryggvason*, 1980] to 2.0 per day for Kilauea [*Dvorak and Okamura*, 1987]. Our estimate for Westdahl is similar, although it is subject to the following uncertainties: (1) the modeled volume change during the first 20 hours of the eruption is based on just one interferogram, (2) our estimate for the volume of the 1991–1992 lava flow is based on an assumed average flow thickness that could be in error by a factor of ~2, and (3) the time constant calculation is based on the steady state volume change in the reservoir inferred from our model rather than on the volume added prior to the 1991–1992 eruption (for which no estimate is available). The important point is that both the deflation rate and the extrusion rate were high during the first few days of the 1991–1992 eruption and both declined substantially thereafter, which fits a pattern that has been documented at other frequently active basaltic shield volcanoes [*Dvorak and Dzurisin*, 1997].

[37] Our results are summarized in Figure 8, which portrays an eruption cycle that is based on fluid flow principles. A magma reservoir about 6 km below sea level inflates at an exponentially declining rate for several years before an eruption (or intrusion), ruptures when some unspecified threshold is attained, then deflates at an exponentially declining rate for a few days during the eruption. The cycle then repeats, producing a series of eruptions or intrusions with similar repose intervals and volumes. Eventually, the pattern is broken by some change in the plumbing system, local stress field, or any other factor that changes the rupture threshold. Magma accumulation occurs mainly below the brittle-ductile transition, which typically occurs ~5 km beneath volcanoes, so the slow ascent of magma to that depth generally is not marked by earthquakes [*Hill*, 1992; *Sibson*, 1982].

Figure 6. (opposite) (a) Estimated source positions, superimposed on a shaded-relief image of Westdahl volcano, are shown with uncertainty ellipses at 1σ. Cross indicates the weighted average position, which is nearly centered on the active vent of Westdahl Peak. (b) Estimated volume change and depth of magma reservoir using the average location of modeled sources. Error bars and circles represent 1σ uncertainties for depth and volume change of the source, respectively. The weighted average depth (the heavy dotted line) is about 5.8 km below sea level (7.3 km beneath the summit). Gray vertical line represents the eruption onset on 29 November 1991. An epoch that includes the first 20 hours of the eruption is not included in the average depth estimation. (c) Estimated volume changes for different epochs using the fixed average location and depth of the magma reservoir. Error bars represent 1σ uncertainties.

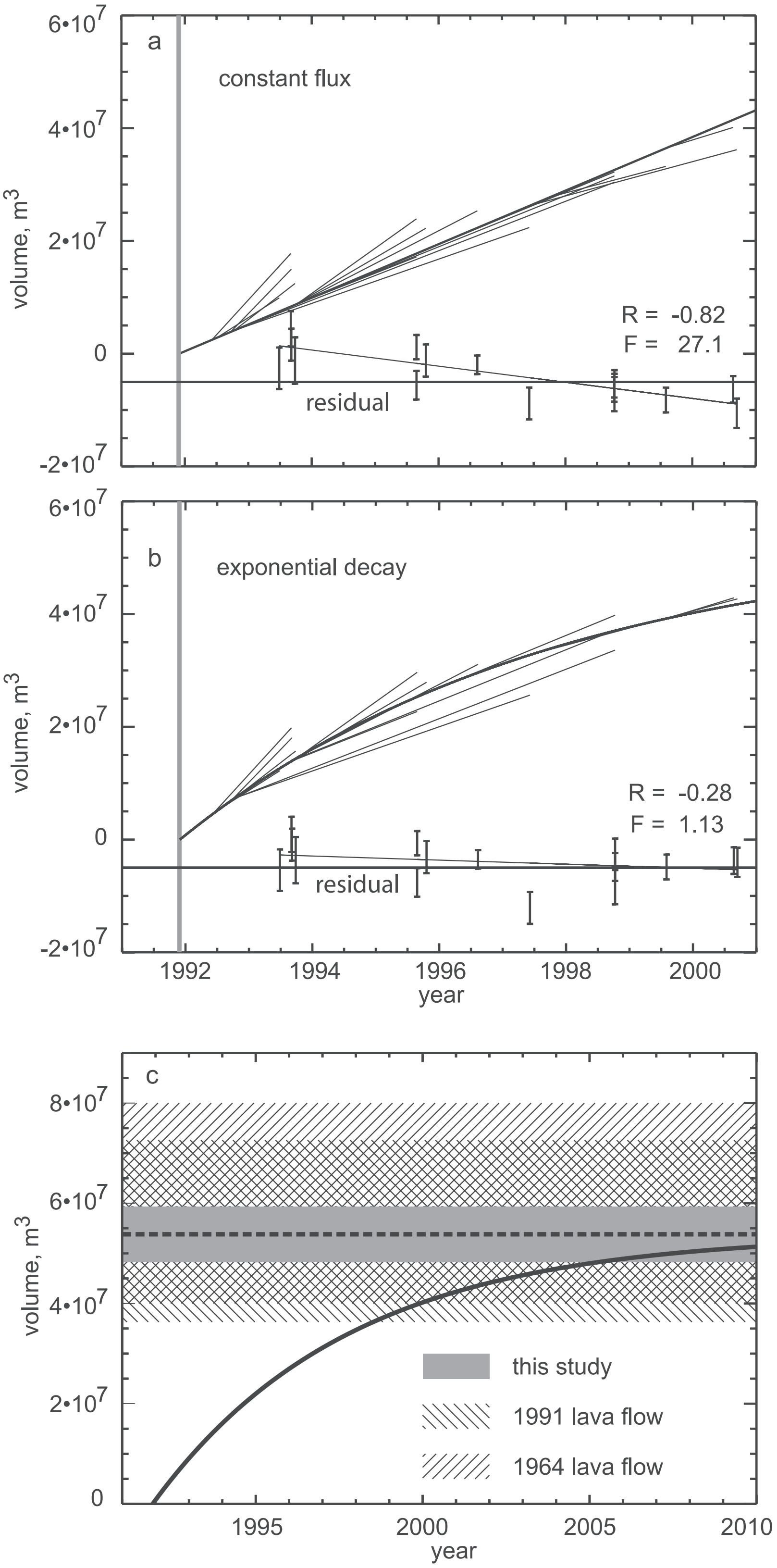
a
constant flux
R = -0.82
F = 27.1
residual
b
exponential decay
R = -0.28
F = 1.13
residual
volume, m3
6•10^7
4•10^7
2•10^7
0
-2•10^7
1992
1994
1996
1998
2000
year
c
8•10^7
6•10^7
4•10^7
2•10^7
0
1995
2000
2005
2010
this study
1991 lava flow
1964 lava flow

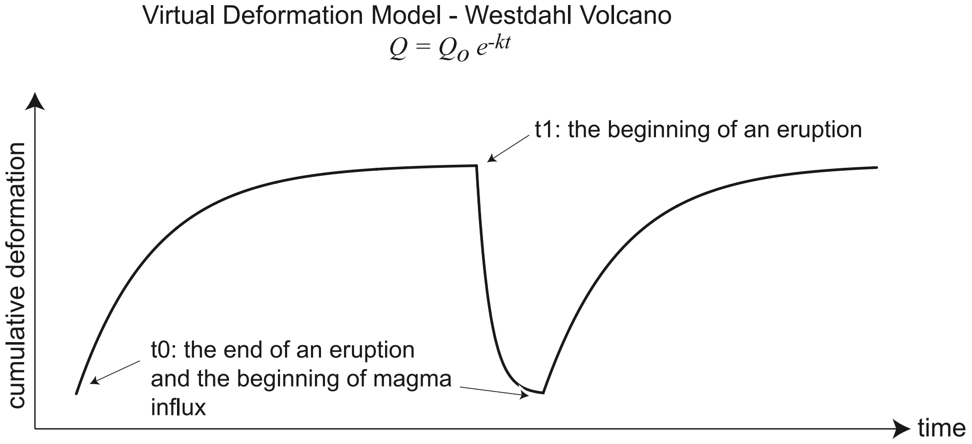

Figure 8. A model for the eruption cycle at Westdahl volcano. The model is based on observed deformation rates and principles of fluid flow from a constant pressure source through a conduit to an elastic reservoir. The model predicts that the rates of inflation and deflation decay exponentially with very different time constants. If the reservoir ruptures at the same point in each cycle, the result is a series of eruptions at regular intervals and with similar volumes. Recent eruptions at Westdahl seem to fit such a pattern.

[38] Although such a model could, in theory, be used to predict future eruptions, this is difficult in practice for at least two reasons. First, the model inflation rate decays exponentially with time and approaches zero as a limit. In theory therefore the surface displacement rate likewise declines, and the system gradually approaches a steady state. At volcanoes that erupt frequently, such as Westdahl, some unknown threshold is attained before the inflation rate is diminished, causing the reservoir to rupture and producing an eruption or intrusion. Relatively long-term predictions based solely on declining deformation rates would pose a particularly difficult challenge. On the other hand, recognition of aseismic inflation at an otherwise quiescent volcano provides a rationale for enhanced geodetic, seismic, and volcanic gas monitoring, which should detect the onset of shallow intrusion and provide a basis for shorter-term predictions [e.g., *McNutt et al.*, 2000].

[39] A second difficulty with using the model as a predictive tool is that volcanoes are remarkably complex systems that are subject to disturbance by various internal and external influences, including changes in the deep magma production zone, structural changes caused by eruptions, physical, and chemical changes in magma bodies, distant earthquakes, and regional stress changes. Each of these factors can perturb the delicate balance between magma supply, storage, and eruption that is required to produce the regular behavior inherent in the model, either by introducing time dependency in the model parameters or by invalidating the model entirely. There is no reason to expect, for example, that the model parameters we deduced by fitting equation (5) to modeled volume changes during 1991–2000 are appropriate to describe Westdahl's behavior either long before or long after the period spanned by our study. The volcano has behaved differently in the past, and it will surely behave differently sometime in the future. It would not be reasonable to expect the same model to describe the behavior of other volcanoes, given the complexity of most magmatic systems. Experience shows that most volcanoes do not exhibit strictly repetitive behavior most of the time, so the model developed here cannot be generally applicable.

[40] On the other hand, some volcanoes do exhibit repetitive behavior some of the time, and in these cases the model might be useful for anticipating eruptions or recognizing when the pattern has changed. For example, the intervals between Westdahl's last three eruptions have been 14 and 13 years, and the erupted volumes are probably the

Figure 7. (opposite) (a) In the upper part of the figure, changes in source volume were fit to a constant flux model. In the lower part of the figure, residuals between the estimated volume changes and the predicted ones that are based on the constant flux model are given. Because the slope of the regression line (dashed line) that fits the residuals deviates significantly from the null hypothesis (thick horizontal line), the constant flux model is rejected. The regression has a correlation coefficient $R = -0.82$ and an F test between the regression and the null hypothesis, $F = 27$, is significant. (b) In the upper part of the figure, changes in source volume were fit to a model with exponentially decaying flux. In the lower part of the figure, the residuals between the estimated volume changes and the predicted ones that are based on the exponentially decaying flux model are given. The slope of the regression line (dashed line) that fits the residuals does not deviate significantly from the null hypothesis (thick horizontal line), the regression on the residuals has a correlation coefficient $R = -0.28$, and an F test between the regression and the null hypothesis, $F = 1.1$, is not significant. (c) Magma reservoir volume change as a function of time. The steady state volume in the reservoir inferred from our model (equations (4) and (5)) and its uncertainty at 1σ are shown. The subsurface volume changes for 1964 and 1991–1992 eruptions are estimated from lava flow areal extents and an assumed average lava thickness of 5–10 m and were accounted for the vesicularity.

same within a factor of two. This suggests that the eruption cycle has been more nearly regular than random and that the pattern is likely to repeat itself until the system is perturbed in some way that changes the volcano's behavior. Whether the pattern will remain intact through the next eruption remains to be seen.

5. Conclusions

[41] InSAR has made significant contributions to help us understand the broad spectrum of volcanic activity along the Aleutian arc and has helped scientists plan and prioritize their volcano-monitoring efforts. At Westdahl volcano, multiple InSAR images that span the time period from 1991 to 2000 show the volcano deflated during its 1991–1992 eruption and is reinflating at a rate that could produce another eruption within several years. The rates of inflation and deflation are approximated by exponential decay functions having time constants of about 6 years and a few days, respectively. This behavior is consistent with a deep, constant-pressure magma source connected to a shallow reservoir by a magma-filled conduit. Such a physically based model for magma supply dynamics is consistent with InSAR observations that span a significant fraction of a complete eruption cycle. A similar model has been proposed for other basaltic shield volcanoes and might be applicable elsewhere, especially at volcanoes that erupt frequently and have relatively simple plumbing systems. The model predicts a repeating pattern of eruptions with similar repose intervals and volumes, and it could be refined to produce more realistic patterns for a specific volcano with additional observational constraints.

[42] With the implementation of InSAR technology, volcano monitoring has entered an exciting phase in which magma accumulation in the middle to upper crust can be observed long before the onset of short-term eruption precursors. However, our model suggests that in some cases the magma flux decays exponentially with time, which makes short-term forecasting based on this approach very difficult. Experience shows that short-term precursors, such as localized deformation, seismicity, and changes in gas emission, are observed when the reservoir nears rupture or as magma intrudes overlying rock, typically providing days to months of warning. InSAR is shedding light on a part of the eruption cycle that heretofore had been mostly beyond reach (i.e., the time period between eruptions when a volcano seems to be doing essentially nothing). Better understanding requires observations over a wide range of time and length scales using various sensors and techniques, including InSAR, continuous GPS, gravity, strainmeters, tiltmeters, seismometers, and volcanic gas studies, and also more realistic models of how volcanoes work.

[43] **Acknowledgments.** ERS-1/ERS-2 SAR images are copyright© 1991–2000 ESA and provided by the NASA/ASF. This research was supported by funding from NASA (NRA-99-OES-10 RADARSAT-0025-0056), and in part by the USGS contracts O3CRCN0001 and 1434-CR-97-CN-40274 and the USGS Volcano Hazards Program. The SRTM data were processed by NASA/JPL for NIMA and provided by USGS EROS Data Center. We thank the User Service of ASF for their special efforts to provide SAR data on a timely basis and D-PAF/ESA for providing precise satellite orbit information. We thank the Associate Editor, Freysteinn Sigmundsson, and three reviewers, Nicki Stevens, Makoto Murakami, and Rikke Pedersen for constructive and useful comments and suggestions. We also thank Tina Neal, Game McGimsey, Ken Dean, and John Power for helpful discussions of the 1991 eruption at Westdahl volcano, and Wayne Thatcher and Chengquan Huang for technical reviews.

References

Amelung, F., S. Jonsson, H. Zebker, and P. Segall, Widespread uplift and 'trapdoor' faulting on Galapagos volcanoes observed with radar interferometry, *Nature*, *407*, 993–996, 2000.

Beauducel, F., P. Briole, and J. L. Froger, Volcano-wide fringes in ERS satellite radar interferograms of Etna (1992–1998): Deformation or tropospheric effect?, *J. Geophys. Res.*, *105*, 16,391–16,402, 2000.

Cashman, K. V., M. T. Mangan, and S. Newman, Surface degassing and modifications to vesicle size distributions in active basalt flows, *J. Volcanol. Geotherm. Res.*, *61*, 45–68, 1994.

Christensen, N. I., Poisson's ratio and crustal seismology, *J. Geophys. Res.*, *101*, 3139–3156, 1996.

Davis, J. C., *Statistics and Data Analysis in Geology*, 550 pp., John Wiley, New York, 1973.

Dean, K. G., K. Engle, K. Partington, J. Groves, and J. Dehn, Analysis of surface processes using SAR data: Westdahl volcano, Alaska, *Int. J. Remote Sens.*, *23*, 4529–4550, 2002.

Dvorak, J., and D. Dzurisin, Volcano geodesy: The search for magma reservoirs and the formation of eruptive vents, *Rev. Geophys.*, *35*, 343–384, 1997.

Dvorak, J., and A. T. Okamura, A hydraulic model to explain variations in summit tilt rate at Kilauea and Mauna Loa volcanoes, in *Volcanism in Hawaii*, edited by R. W. Decker, T. L. Wright, and P. H. Stauffer, *U.S. Geol. Surv. Prof. Pap., 1350*, 1281–1296, 1987.

Dzurisin, D., A comprehensive approach to monitoring volcano deformation as a window on the eruption cycle, *Rev. Geophys.*, *41*(1), 1001, doi:10.1029/2001RG000107, 2003.

Farr, T. G., and M. Kobrick, Shuttle Radar Topography Mission produces a wealth of data, *Eos Trans. American Geophysical Union*, *81*(48), 583–585, 2000.

Ferretti, A., C. Prati, and F. Rocca, Nonlinear subsidence rate estimation using permanent scatterers in differential SAR interferometry, *IEEE Trans. Geosci. Remote Sens.*, *38*, 2202–2212, 2000.

Fujiwara, S., P. A. Rosen, M. Tobita, and M. Murakami, Crustal deformation measurements using repeat-pass JERS-1 synthetic aperture radar interferometry near the Izu Peninsula, Japan, *J. Geophys. Res.*, *103*, 2411–2426, 1998.

Gesch, D., Topographic data requirement for EOS global change research, *U.S. Geol. Surv. Open File Rep., 94-626*, 60 pp., 1994.

Global Volcanism Network, *Smithsonian Inst. Bull.*, 1978. (Available at http://www.volcano.si.edu).

Global Volcanism Network, *Smithsonian Inst. Bull.*, 1991. (Available at http://www.volcano.si.edu).

Hensley, S., R. Munjy, and P. Rosen, Interferometric synthetic aperture radar (IFSAR), in *Digital Elevation Model Technologies and Applications: The DEM Users Manual*, edited by D. F. Maune, pp. 143–206, Am. Soc. for Photogramm. and Remote Sens., Bethesda, Md., 2001.

Hill, D. P., Temperatures at the base of the seismogenic crust beneath Long Valley caldera, California, and the Phlegraean Fields caldera, Italy, in *International Association of Volcanology and Chemistry of the Earth's Interior (IAVCEI) Proceedings in Volcanology*, vol. 3, *Volcanic Seismology*, edited by P. Gasparini and R. Scarpa, pp. 433–461, Springer-Verlag, New York, 1992.

Johnson, D. J., F. Sigmundsson, and P. T. Delaney, Comment on "Volume of magma accumulation or withdrawal estimated from surface uplift or subsidence, with application to the 960 collapse of Kilauea volcano" by P. T. Delaney and D. F. McTigue, *Bull. Volcanol.*, *61*, 491–493, 2000.

Jolly, A., et al., Catalog of earthquake hypocenters at Alaskan volcanoes: January 1, 1994 through December 31, 1999, *U.S. Geol. Surv. Open File Rep., 01-189*, 2001.

Jonsson, S., et al., A shallow-dipping dike fed the 1995 flank eruption at Fernandina volcano, Galapagos, observed by satellite radar interferometry, *Geophys. Res. Lett.*, *26*, 1077–1080, 1999.

Lanari, R., P. Lundgren, and E. Sansosti, Dynamic deformation of Etna volcano observed by satellite radar interferometry, *Geophys. Res. Lett.*, *25*, 1541–1544, 1998.

Lockwood, J. P., et al., Mauna Loa 1974–1984: A decade of intrusive and extrusive activity, in *Volcanism in Hawaii*, edited by R. W. Decker, T. L. Wright, and P. H. Stauffer, *U.S. Geol. Surv. Prof. Pap., 1450*, 537–570, 1987.

Lu, Z., R. Fatland, M. Wyss, S. Li, J. Eichelberger, and K. Dean, Deformation of volcanic vents detected by ERS-1 SAR interferometry, Katmai National Park, Alaska, *Geophys. Res. Lett.*, *24*, 695–698, 1997.

Lu, Z., D. Mann, and J. Freymueller, Satellite radar interferometry measures deformation at Okmok Volcano, *Eos Trans. American Geophysical Union*, *79*(39), 461–468, 1998.

Lu, Z., D. Mann, J. Freymueller, and D. Meyer, Synthetic aperture radar interferometry of Okmok volcano, Alaska: Radar observations, *J. Geophys. Res.*, *105*(10), 10,791–10,806, 2000a.

Lu, Z., C. Wicks, D. Dzurisin, W. Thatcher, J. Freymueller, S. McNutt, and D. Mann, Aseismic inflation of Westdahl volcano, Alaska, revealed by satellite radar interferometry, *Geophys. Res. Lett.*, *27*, 1567–1570, 2000b.

Lu, Z., C. Wicks, J. Power, and D. Dzurisin, Ground deformation associated with the March 1996 earthquake swarm at Akutan volcano, Alaska, revealed by satellite radar interferometry, *J. Geophys. Res.*, *105*, 21,483–21,496, 2000c.

Lu, Z., C. Wicks, D. Dzurisin, J. Power, S. Moran, and W. Thatcher, Magmatic inflation at a dormant stratovolcano: 1996–1998 activity at Mount Peulik volcano, Alaska, revealed by satellite radar interferometry, *J. Geophys. Res.*, *107*(B7), 2134, doi:10.1029/2001JB000471, 2002a.

Lu, Z., J. Power, V. McConnell, C. Wicks, and D. Dzurisin, Pre-eruptive inflation and surface interferometric coherence characteristics revealed by satellite radar interferometry at Makushin volcano, Alaska: 1993–2000, *J. Geophys. Res.*, *107*(B11), 2266, doi:10.1029/2001JB000970, 2002b.

Lu, Z., T. Masterlark, J. Power, D. Dzurisin, and C. Wicks, Subsidence at Kiska volcano, western Aleutians, detected by satellite radar interferometry, *Geophys. Res. Lett.*, *29*(18), 1855, doi:10.1029/2002GL014948, 2002c.

Lu, Z., C. Wicks, J. Power, D. Dzurisin, W. Thatcher, and T. Masterlark, Interferometric synthetic aperture radar studies of Alaska volcanoes, *Proc. Int. Geosci. Remote Sens. Symp., Toronto*, 191–194, 2002d.

Lu, Z., E. Fielding, M. Patrick, and C. Trautwein, Estimating lava volume by precision combination of multiple baseline spaceborne and airborne interferometric synthetic aperture radar: The 1997 eruption of Okmok volcano, Alaska, *IEEE Trans. Geosci. Remote Sens.*, in press, 2003a.

Lu, Z., C. Wicks, D. Dzurisin, J. Power, W. Thatcher, and T. Masterlark, Interferometric synthetic aperture radar studies of Alaska volcanoes, *Earth Obs. Mag.*, *12*(3), 8–18, 2003b.

Mann, D., and J. Freymueller, Volcanic and tectonic deformation on Unimak Island in the Aleutian Arc, Alaska, *J. Geophys. Res.*, *108*(B2), 2108, doi:10.1029/2002JB001925, 2003.

Mann, D., J. Freymueller, and Z. Lu, Deformation associated with the 1997 eruption of Okmok volcano, Alaska, *J. Geophys. Res.*, *107*(B4), 2072, 10.1029/2001JB000163, 2002.

Massonnet, D., and K. Feigl, Radar interferometry and its application to changes in the Earth's surface, *Rev. Geophys.*, *36*, 441–500, 1998.

Massonnet, D., P. Briole, and A. Arnaud, Deflation of Mount Etna monitored by spaceborne radar interferometry, *Nature*, *375*, 567–570, 1995.

McCann, G. D., and C. H. Wilts, A mathematical analysis of the subsidence in the Long Beach-San Pedro Area, report, Calif. Inst. of Technol., Pasadena, Calif., 1951.

McNutt, S., H. Rymer, and J. Stix, Synthesis of volcano monitoring, in *Encyclopedia of Volcanoes*, edited by H. Sigurdsson et al., pp. 1165–1184, Academic, San Diego, Calif., 2000.

Menke, W., *Geophysical Data Analysis: Discrete Inverse Theory*, *Int. Geophys. Ser.*, vol. 45, 289 pp., Academic, San Diego, Calif., 1989.

Miller, T. P., et al., Catalog of the historically active volcanoes of Alaska, *U.S. Geol. Surv. Open File Rep., 98-582*, p. 104, 1998.

Mogi, K., Relations between the eruptions of various volcanoes and the deformations of the ground surface around them, *Bull. Earthquake Res. Inst. Univ. Tokyo*, *36*, 99–134, 1958.

Murakami, M., M. Tobita, S. Fujiwara, T. Saito, and H. Massaharu, Coseismic crustal deformations of 1994 Northridge California earthquake detected by interferometric JERS-1 SAR, *J. Geophys. Res.*, *101*, 8605–8614, 1996.

Newhall, C. G., and S. Self, The volcanic explosivity index (VEI): An estimate of explosive magnitude for historical volcanism, *J. Geophys. Res.*, *87*, 1231–1238, 1982.

Press, W., S. Teukolsky, W. Vetterling, B. Flannery, *Numerical Recipes in C, the Art of Scientific Computing*, 994 pp., Cambridge Univ. Press, New York, 1992.

Rosen, P. A., et al., Synthetic aperture radar interferometry, *Proc. IEEE*, *88*, 333–380, 2000.

Rowland, S. K., G. A. Smith, and P. J. Mouginis-Mark, Preliminary ERS-1 observations of Alaskan and Aleutian volcanoes, *Remote Sens. Environ.*, *48*, 358–369, 1994.

Sibson, R., Fault zone models, heat flow, and the depth distribution of seismicity in the continental crust of the United States, *Bull. Seismol. Soc. Am.*, *72*, 151–163, 1982.

Sigmundsson, F., H. Vadon, and D. Massonnet, Readjustment of the Krafla spreading segment to crustal rifting measured by satellite radar interferometry, *Geophys. Res. Lett.*, *24*, 1843–1846, 1997.

Sigmundsson, F., P. Durand, and D. Massonnet, Opening of an eruptive fissure and seaward displacement at Piton de la Fournaise volcano measured by RADARSAT satellite radar interferometry, *Geophys. Res. Lett.*, *26*, 533–536, 1999.

Simkin, T., and L. Siebert, *Volcanoes of the World*, 2nd ed., 349 pp., Geosci. Press, Inc., Tucson, 1994.

Stevens, N. F., G. Wadge, C. A. Williams, J. G. Morley, J. P. Muller, J. B. Murray, and M. Upton, Surface movements of emplaced lava flows measured by synthetic aperture radar interferometry, *J. Geophys. Res.*, *106*, 11,293–11,313, 2001.

Thatcher, W., and D. Massonnet, Crustal deformation at Long Valley Caldera, eastern California, 1992–1996, inferred from satellite radar interferometry, *Geophys. Res. Lett.*, *24*, 2519–2522, 1997.

Tryggvason, E., Subsidence events in the Krafla area, North Iceland, 1975–1979, *J. Geophys.*, *47*, 141–153, 1980.

Wicks, C., Jr., W. Thatcher, and D. Dzurisin, Migration of fluids beneath Yellowstone Caldera inferred from satellite radar interferometry, *Science*, *282*, 458–462, 1998.

Wicks, C., Jr., D. Dzurisin, S. Ingebritsen, W. Thatcher, Z. Lu, and J. Iverson, Magmatic activity beneath the quiescent Three Sisters volcanic center, central Oregon Cascade Range, USA, *Geophys. Res. Lett.*, *29*(7), 1122, 10.1029/2001GL014205, 2002.

Williams, C. A., and G. Wadge, The effects of topography on magma reservoir deformation models: Application to Mt. Etna and radar interferometry, *Geophys. Res. Lett.*, *25*, 1549–1552, 1998.

Wood, C. A., and J. Kienle, *Volcanoes of North America: United States and Canada*, 354 pp., Cambridge Univ. Press, New York, 1990.

Zebker, H., F. Amelung, and S. Jonsson, Remote sensing of volcano surface and internal processing using radar interferometry, in *Remote Sensing of Active Volcanism*, *Geophys. Monogr. Ser.*, vol. 116, edited by P. Mougins-Mark, J. A. Crisp, and J. H. Fink, pp. 179–205, AGU, Washington, D. C., 2000.

D. Dzurisin, U.S. Geological Survey, David A. Johnston Cascades Volcano Observatory, 1300 SE Cardinal Court, Building 10, Suite 100, Vancouver, WA 98683-9589, USA. (dzurisin@usgs.gov)

Z. Lu, T. Masterlark, and R. Rykhus, U.S. Geological Survey, EROS Data Center, SAIC, 47914, 252nd Street, Sioux Falls, SD 57198, USA. (lu@usgs.gov; masterlark@usgs.gov; rykhus@usgs.gov)

C. Wicks Jr., U.S. Geological Survey, 345 Middlefield Road, MS 977, Menlo Park, CA 94025-3591, USA. (cwicks@usgs.gov)

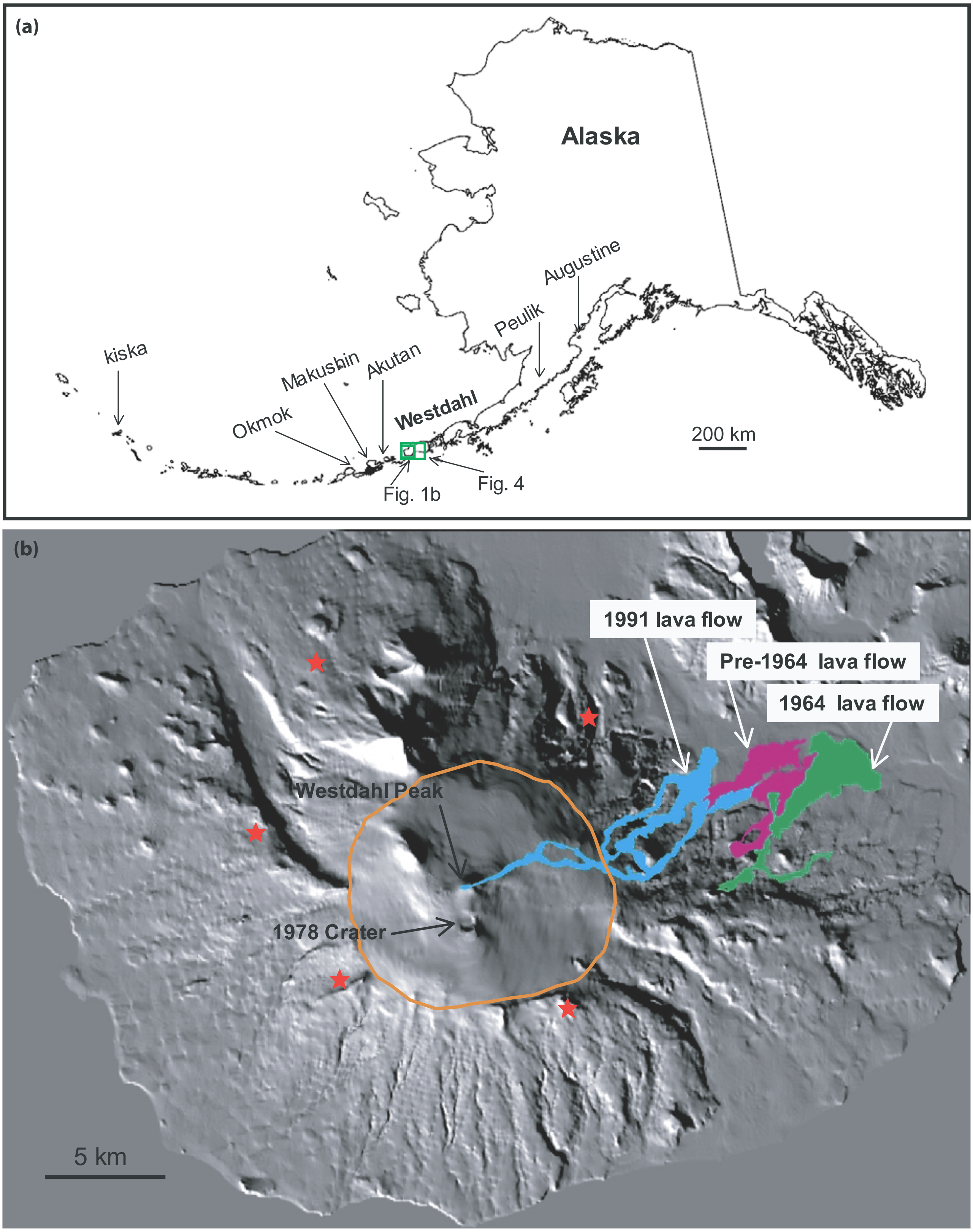

Figure 1. (a) Map of Alaska including the 2500-km long Aleutian volcanic arc. Rectangles outline areas are shown in Figures 1b and 4. (b) Shaded-relief image of Westdahl volcano. The 1978 crater, the Westdahl Peak (1991–1992 eruption vent), and the lava flows from pre-1964, 1964, and 1991 eruptions are labeled. Stars denote locations of seismic stations near the volcano. The glacier on the volcano is outlined in orange.

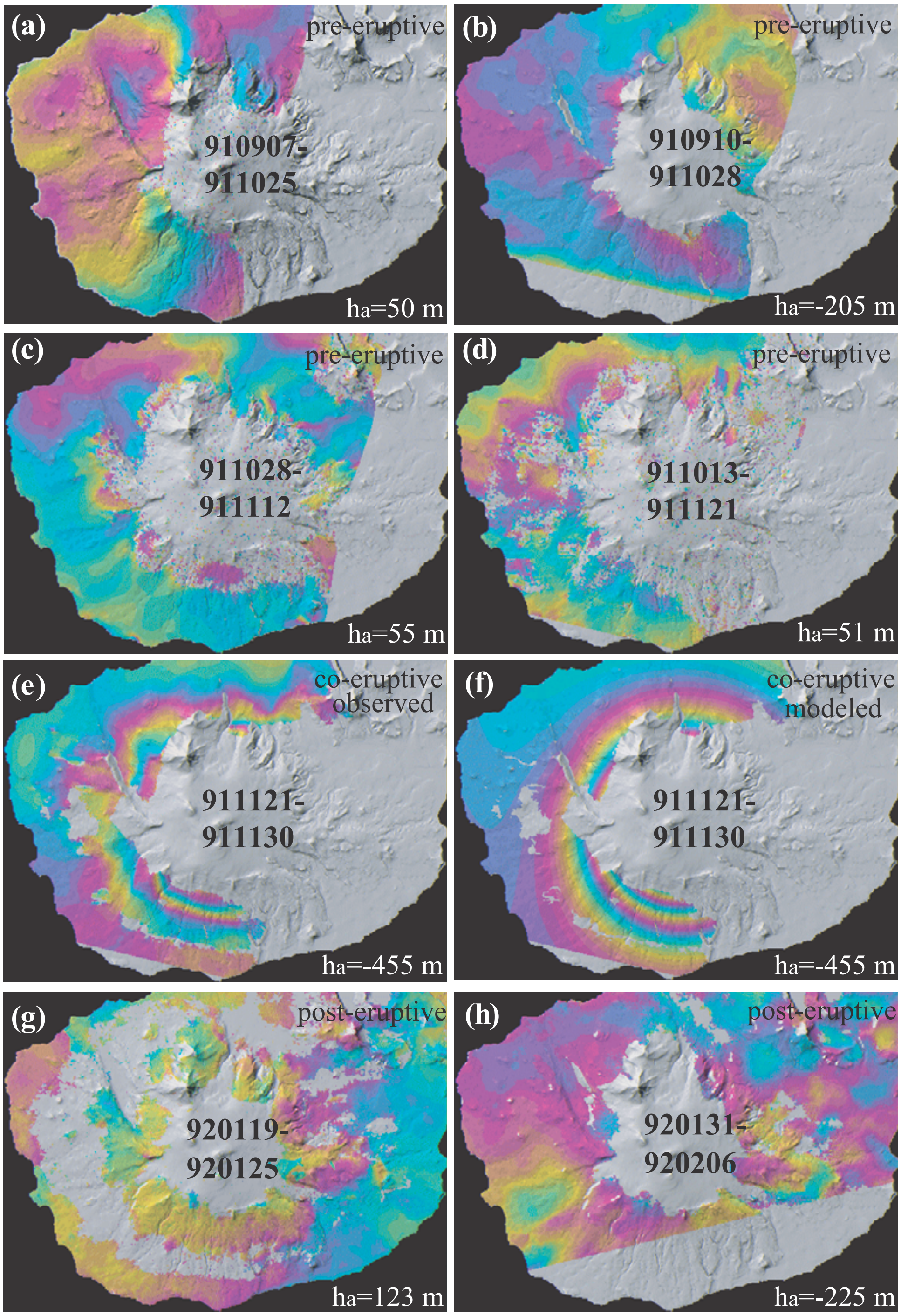

Figure 2. Observed (a–e, g, h) and modeled (f) interferograms for time periods soon before (Figures 2a–2d), including (Figures 2e, 2f), and after (Figures 2g, 2h) the start of an eruption on 29 November 1991. Topographic effects have been removed using a DEM. Each fringe (full color cycle) represents 2.83 cm of range change between the ground and the satellite. Additional information on SAR images used for the interferograms is given in Table 1. Each interferogram covers the same area as Figure 1b. The altitude of ambiguity, h_a, for each interferogram is labeled. Figures 2e and 2f show observed and modeled deflation, respectively, during the first 20 hours of the eruption. Areas that lack interferometric coherence are uncolored.

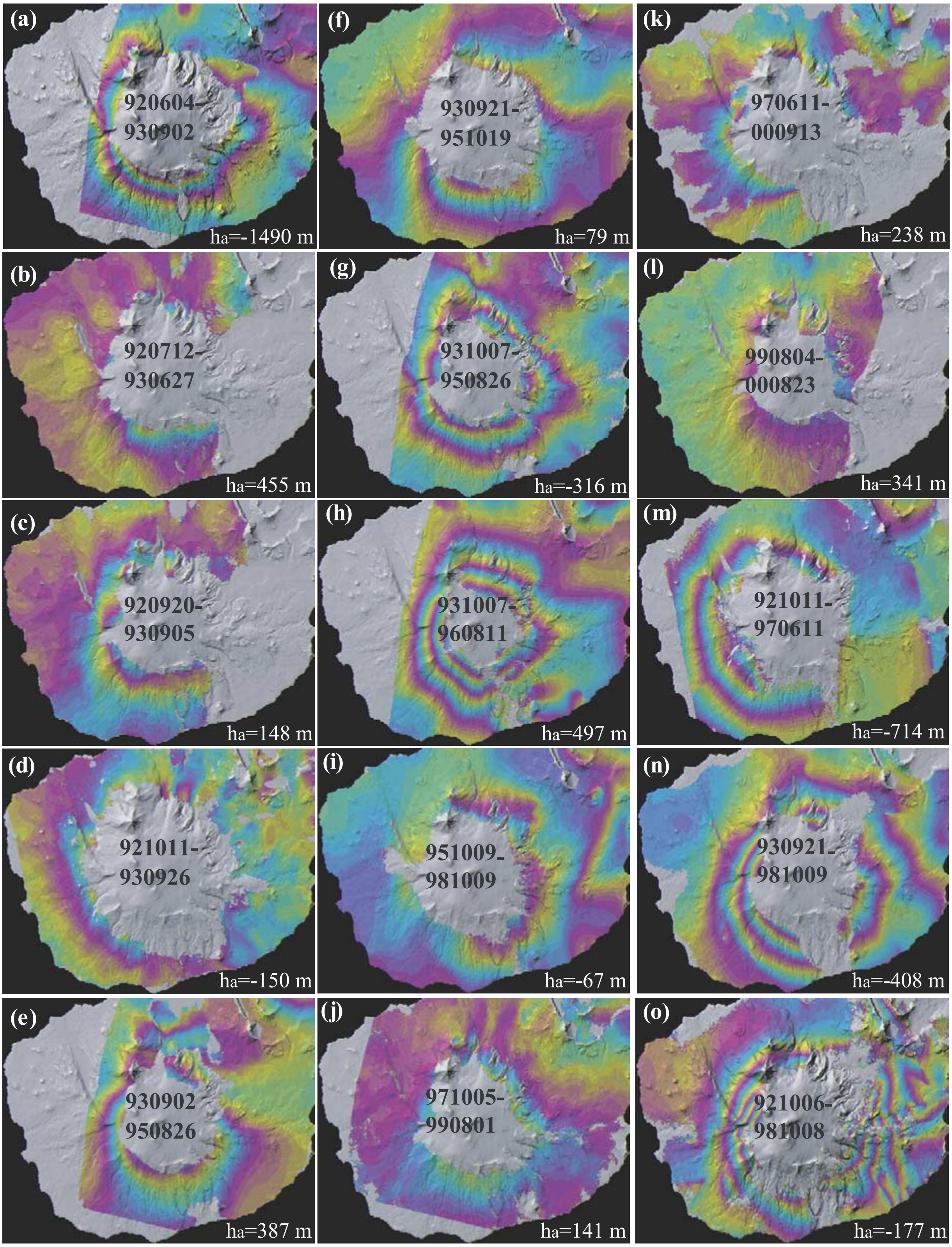

Figure 3. Observed interferograms for various time windows during 1991–2000 starting after the 1991–1992 eruption and showing progressive inflation. Each fringe (full color cycle) represents 2.83 cm of range change between the ground and the satellite. Additional information on SAR images used for the interferograms is given in Table 1. Each interferogram covers the same area as Figure 1b. The altitude of ambiguity, h_a, for each interferogram is labeled. Areas that lack interferometric coherence are uncolored.

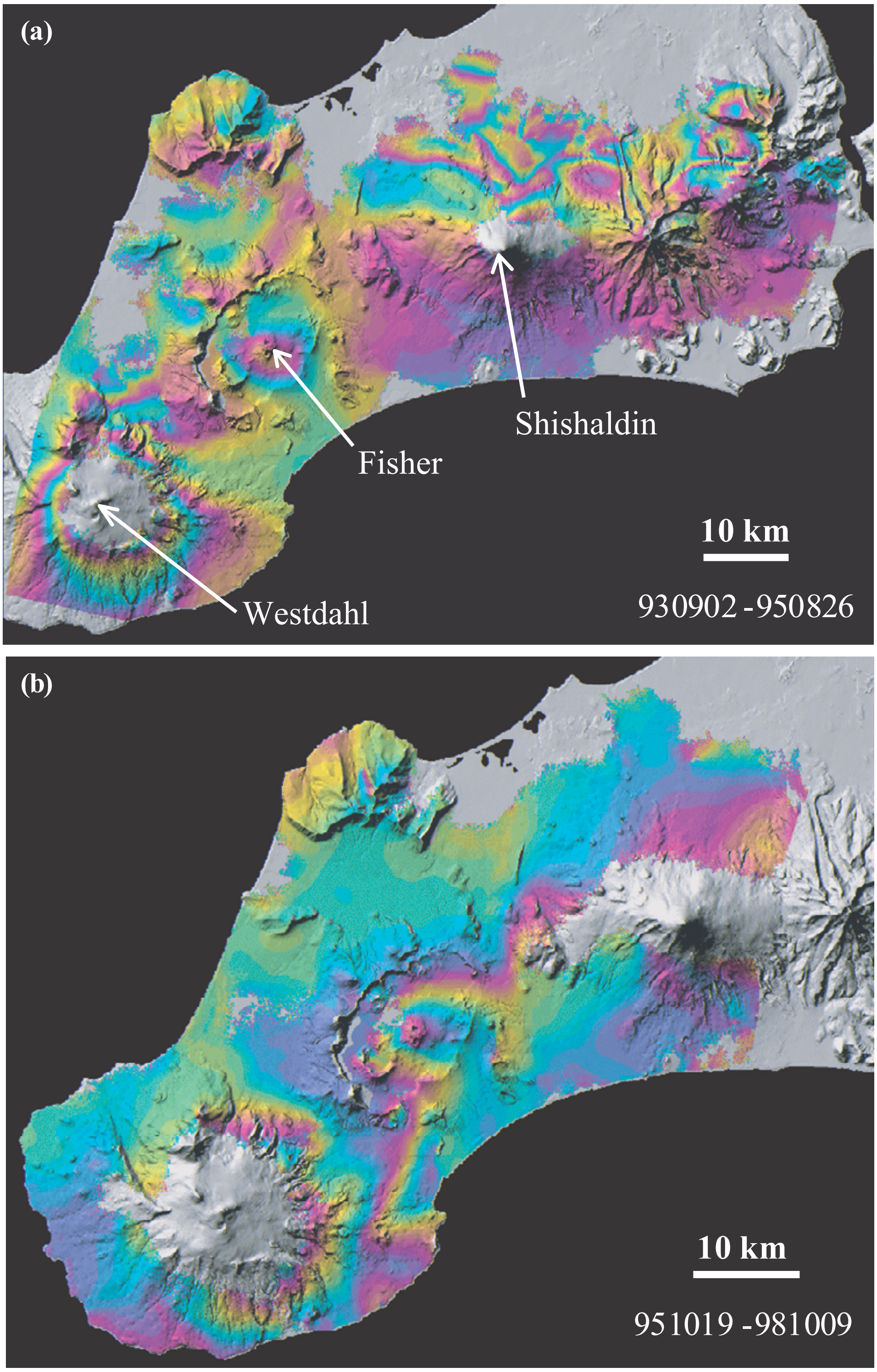

Figure 4. Observed interferograms of the western part of Unimak Island showing the effects of atmospheric delay anomalies (see text). (a) This image was produced from the same SAR images used for Figure 3e, but this version covers a larger area. (b) Same as Figure 3i, but a larger area. One fringe (a full color cycle) represents the range change of 2.83 cm. Outlines of these two images are shown in Figure 1a. Peaks of Westdahl (elevation of ~1550 m), Fisher (elevation of ~500 m), and Shishaldin (elevation of ~2800 m) are labeled in Figure 4a.

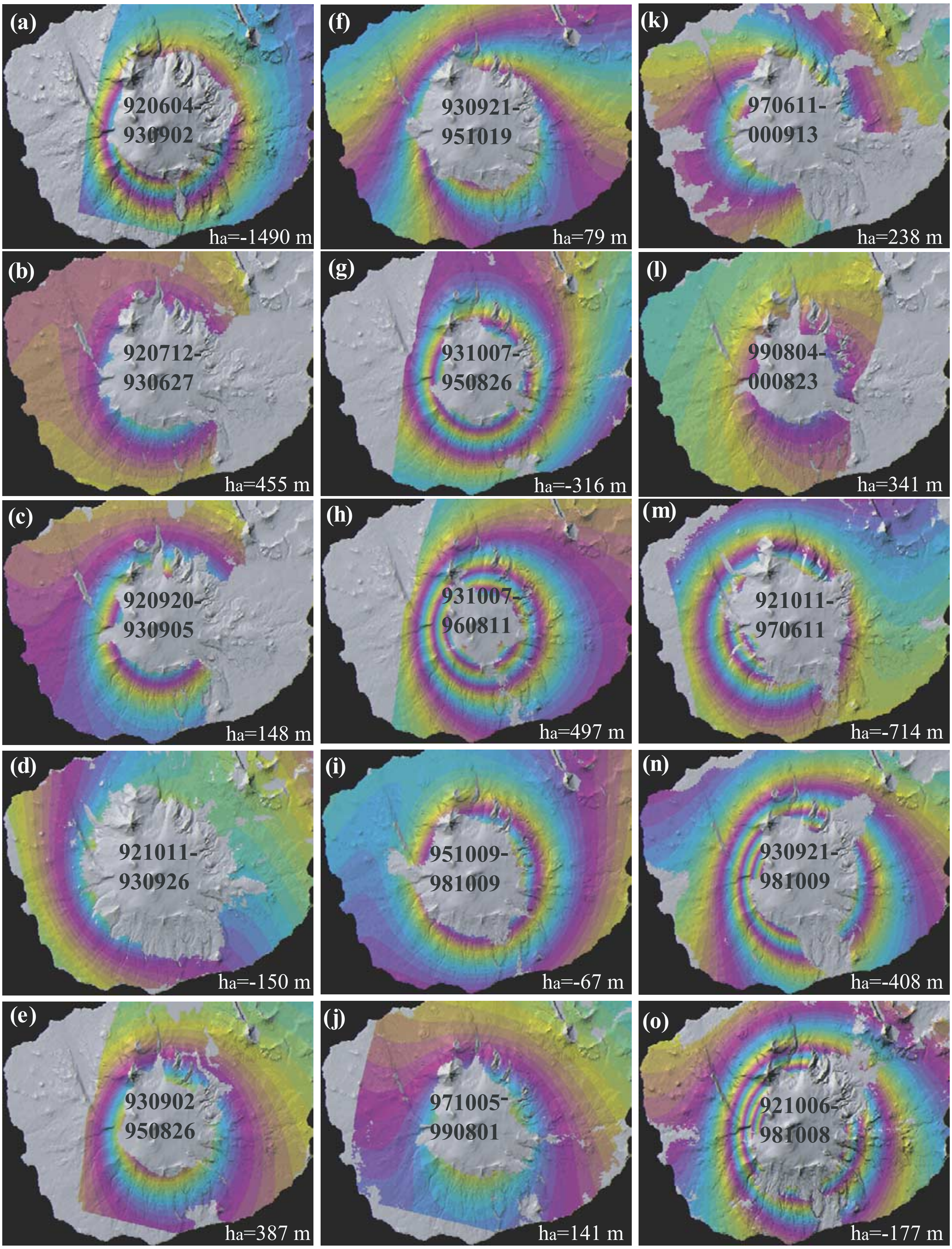

Figure 5. Modeled interferograms that correspond to the observed images in Figure 3. These synthetic interferograms were produced using the corresponding best fit sources from a model described in the text. Each fringe (full color cycle) represents 2.83 cm of range change between the ground and the satellite. The altitude of ambiguity, h_a, for each interferogram is labeled. Areas that lack interferometric coherence are uncolored.